Recycling Valuable Materials from

Crystalline-Si Solar Modules

by

Wen-Hsi Huang

A Dissertation Presented in Partial Fulfillment
of the Requirements for the Degree
Doctor of Philosophy

Approved February 2018 by the
Graduate Supervisory Committee:

Meng Tao, Chair
Terry Alford
Parikhit Sinha

ARIZONA STATE UNIVERSITY

May 2018

ABSTRACT

A major obstacle to sustainable solar technologies is end-of-life solar modules. In this thesis, a recycling process is proposed for crystalline-Si solar modules. It is a three-step process to break down Si modules and recover various materials. Over 95% of a module by weight can be recovered with this process. Two new technologies are demonstrated to enable the proposed recycling process. One is sequential electrowinning which allows multiple metals to be recovered one by one from Si modules, Ag, Pb, Sn and Cu. The other is sheet resistance monitoring by the 4-point probe which maximizes the amount of solar-grade Si recovered from Si modules with high throughput. The purity of the recovered metals is above 99% and the recovery rate can achieve between 70~80%. The recovered Si meets the specifications for solar-grade Si and at least 91% of Si from c-Si solar cells can be recovered. The recovered Si and metals are new feedstocks to the solar industry and generate over $12/module in revenue. This revenue enables a profitable recycling business for Si modules without any government support. The chemicals for recycling are carefully selected to minimize their environmental impact and also the cost. A network for collecting end-of-life solar modules is proposed based on the current distribution network for solar modules to contain the collection cost. As a result, the proposed recycling process for c-Si modules is technically, environmentally and financially sustainable.

ACKNOWLEDGMENTS

First I would like to thank Dr. Meng Tao for his continuous support and guidance of my Ph.D. His patient, enthusiasm, systematic supervision, immense knowledge and wealth of motivation help me a lot during my Ph.D. study and for my future career.

I would also like to acknowledge Dr. Alford, Dr. Sinha for serving in my doctoral committee. I sincerely appreciate their valuable opinions, encouragement and questions which can excite me to widen my research with different perspectives. I also acknowledge Dr. Goryll for helping me with the ECV measurement.

I would like to acknowledge all of my colleagues, Woojung Shin, Laidong Wang and Wen-Cheng Sun in the research group. I benefited greatly from the technical discussions with them, which inspired many wonderful ideas to assist me to finish the research.

Last but not the least, I would like to thank my family: my parents, my brother and my friends for supporting me spiritually throughout writing this thesis and my life in general.

TABLE OF CONTENTS

Page

LIST OF TABLES v

LIST OF FIGURES vi

CHAPTER

1 INTRODUCTION 1

1.1 Background 1

1.2 Crystalline-Si Solar Cells and Module Introduction 2

1.3 Previous Works on Recycling Crystalline-Si Solar Modules 6

1.4 Chapter Outline 8

2 INCENTIVES TO RECYCLE CRYSTALLINE-Si MODULES 10

2.1 What to Recycle? 10

2.2 Revenue from Crystalline-Si Modules Recycle 11

2.3 Network for Collecting Solar Modules 11

3 PROPOSED PROCESS TO RECYCLE CRYSTALLINE-Si MODULES 13

3.1 Overview of Proposed Process to Recycle Crystalline-Si Solar Modules 13

3.2 Techniques Introduction for Recycle 17

4 INTRODUCTION OF EQUIPMENTS FOR RECYCLE 19

4.1 4-point Probe 19

4.2 Scanning Electron Microscope (SEM) 23

4.3 Electrochemical Capacitance-Voltage (ECV) 28

5 RECYCLE METALS FROM CRYSTALLINE-Si SOLAR MODULES 32

5.1. Introduction 32

CHAPTER Page

5.2 Metal Dissolution from Crystalline-Si Solar Modules.....33

5.3 Sequential Electrowinning.....36

5.4 Experimental.....38

5.5 Results and Discussions.....41

5.6 Metal Recycle for Crystalline-Si Solar Modules on a Large Scale.....50

5.7 Summary.....52

6 RECYCLE SOLAR GRADE Si FROM C-Si SOLAR CELLS..... 53

6.1 Introduction.....53

6.2 Experimental.....58

6.3 Results and Discussion.....59

6.4 Scanning Electron Microscope for Proving BSF p+ Si Removal.....67

6.5 Characterization of ECV on BSF.....71

6.6 Summary.....74

7 CONCLUSION..... 75

REFERENCES.....76

LIST OF TABLES

Table Page

1. 5.1 Metal Contents in Crystalline-Si Solar Modules by Weight.....36

2. 5.2 Metal Contents in Leaching Solution After Cu Recovery for 48 Hours 48

LIST OF FIGURES

Figure Page

1. 1.1 Percentage of Annual Production for Different Solar Technologies in 2016...1
2. 1.2 Schematic of the Working Principle for a C-Si Solar Cell.....3
3. 1.3 Topview of a c-Si Solar Cell (a) the Composition of a C-Si Solar Module (b)5
4. 2.1 A Collection Network for Solar Module Recycling Based on the Current Distribution Network.....12
5. 3.1 A Proposed Process to Break Down C-Si Solar Modules and Recover Various Materials. 14
6. 3.2 Self-Limited Chemistries for Cell Recycling: Before HNO_3 (a); After HNO_3 (b); After HF (c) and After NaOH (d). 16
7. 4.1 Schematic of 4-Point Probe.....19
8. 4.2 Circuit Diagram for a 4-Point Probe Measurement.....20
9. 4.3 Circuit Diagram for a 2-Point Measurement. 21
10. 4.4 Schematic of the Spreading Current from a 4-Point Probe.....23
11. 4.5 Signals from the Specimen Interacted with Electron Beams in SEM 24
12. 4.6 The Generation of Characteristic X-Rays by SEM. 27
13. 4.7 The Spatial Resolution of the Signals by SEM 28
14. 4.8 Schematic of Capacitance-Voltage (C-V) Measurement. 30
15. 4.9 Schematic of ECV Profiler Setup. 31
16. 5.1 Top View of Solar Cells with Interconnected Wires (a) Cross Section of Cells with Interconnected Wires (b). 33
17. 5.2 Flow Chart of the Metal Dissolution from C-Si Solar Modules.....34

Figure Page

18. 5.3 Schematic of the Three-Electrode System for Sequential Electrowinning of Multiple Metals. 37

19. 5.4 Voltage versus Time for Linear Sweep Voltammetry (a) Current versus Voltage for Linear Sweep Voltammetry (b). 38

20. 5.5 The HNO3 Leaching Solution After Dissolution of Four Metals, Ag, Pb, Sn and Cu....40

21. 5.6 Voltammetry of the Leaching Solution (a) and Zoom-In of (a) between 0.5 V and 0 V vs. Ag/AgCl (b). 42

22. 5.7 EDX Spectra of the Deposits on the Ti Working Electrode Under Different Voltages vs. Ag/AgCl. 43

23. 5.8 Current-Time Plot for Ag Recovery at 0.3 V on the Ti Working Electrode vs. Ag/AgCl. 44

24. 5.9 EDX Spectrum of the Deposit on the Ti Working Electrode at 0.3 V vs. Ag/AgCl for 20,000 s....45

25. 5.10 Comparison of Voltammetry of the Leaching Solution Before and After Ag Recovery. 46

26. 5.11 EDX Spectrum of the Deposit on the Ti Working Electrode at –0.3 V vs. Ag/AgCl for 24 Hrs. 46

27. 5.12 EDX Spectrum of the Deposit on the Pt Counter Electrode After Cu Recovery for 24 Hrs....48

28. 5.13 Scaling up for Metal Recycling from C-Si Solar Modules. 51

29. 6.1 Schematic of POCl3 Diffusion by Diffusion Furnace....54

Figure Page

30. 6.2 Schematic for the Screen Printing and Firing for C-Si Solar Cells: Before Al Printing (a); After Al Printing (b); Firing (c); Cooling (d); Finish (e) 56

31. 6.3 Process Flow for Solar Grade Si Recycle from C-Si Solar Cells 58

32. 6.4 Thickness Loss of Si in NaOH Solutions of Various Concentrations at 25˚C (a) and with or Without HF Pretreatment (b).....60

33. 6.5 Thickness Loss of Si in 1%, 3%, 5% and 10% NaOH Aqueous Solutions at 25˚C.....62

34. 6.6 Si Etch Rate in 1%, 3%, 5% and 10% NaOH Aqueous Solutions at 25˚C. .62

35. 6.7 Thickness Loss of Si in a 3% NaOH Aqueous Solution at 50˚C.....64

36. 6.8 Reciprocal Sheet Resistance of a Si Cell in a 3% NaOH Solution at 50˚C as a Function of Etch Time.....66

37. 6.9 Remaining Weight of a Si Cell in a 3% NaOH Solution at 50˚C as a Function of Etch Time.....67

38. 6.10 Principle of Contrast Between P^+ and P Si Under SEM 68

39. 6.11 SEM Images for BSF P^+ and P Si Contrast Under Different NaOH Etch Time (a) the Average BSF P^+ Si Thickness Versus Etch Time (b).....70

38. 6.12 I-V Curve of Si Part in the C-Si Solar Cell After 30 Min NaOH Etch.....71

38. 6.13 Capacitance Measurement for Si Part of C-Si Solar Cells with 30 Min NaOH Etch. 72

38. 6.14 Carrier Profile of Si Part of C-Si Solar Cells After 30 Min NaOH Etch....73

CHAPTER 1

INTRODUCTION

1.1. Background

Renewable energy becomes an important energy source in recent years. According to the data from international energy agency (IEA) [1], photovoltaics capacity in the world increased about 50% to achieve 75 GW in 2016. A major obstacle on the horizon to sustainable solar technologies is end-of-life solar modules. As module deployment expands rapidly, so will module waste.

Fig. 1.1 shows the percentage of the annual production for different kinds of solar modules in 2016 [2]. Crystalline-Si (c-Si) solar modules including mono-Si modules and multi-Si modules have always been the dominant technology with a ~90% market share. In 2016, the production of c-Si modules reached 77.7 GW_p. This is equal to over 310 million modules, as c-Si modules are 250 Wp each typically.

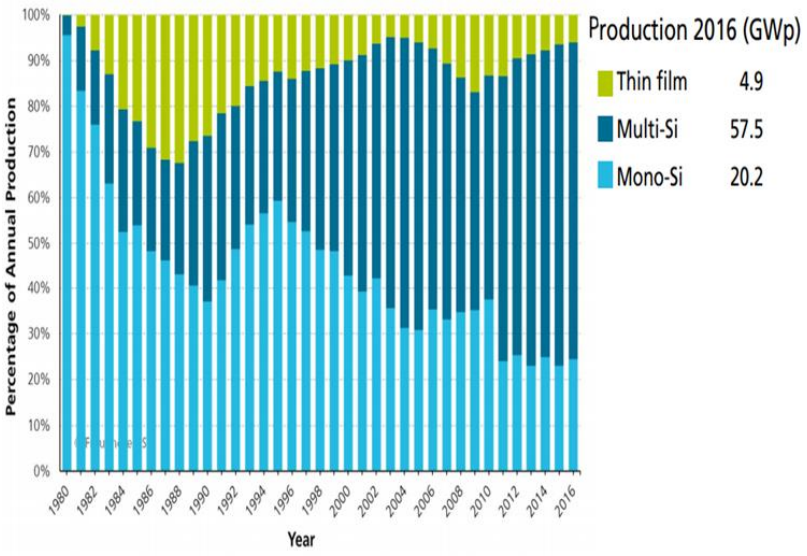

Fig. 1.1 Percentage of annual production for different solar technologies in 2016 [2].

The power of solar modules will degrade after deployment. There are couple mechanisms of degradation such as light-induced degradation, UV-induced degradation, potential-induced degradation, moisture corrosion…etc [3,4]. When the power of modules declines about 20% of the original power, the modules are categorized as end-of-life modules which will be decommissioned [5]. The average lifetime of c-Si solar modules is around 20-25 years depending on the area where they are deployed [5]. With 25-year lifetime, the c-Si solar modules in 2016 would be decommissioned in around 2040. The International Renewable Energy Agency estimates that waste modules will appear in large quantities by the early 2030's and by 2050, they will total 78 million tonnes. The c-Si solar modules contribute to the most of the waste modules.

Since c-Si solar modules occupy~90% market share and they have their lifetime, in the future there will be a huge amount of c-Si solar modules wastes. As a result, a process is needed to take care of these end-of-life c-Si solar modules.

1.2 Crystalline-Si Solar Cells and Module Introduction

The working principle of solar cells is that sunlight absorbed by the p-n junction excites the electron-hole pairs in the semiconductors. The electron-hole pairs can be driven by the built-in voltage of the p-n junction to the outside circuits to provide the power. Fig. 1.2 is the cross section of a commercial c-Si solar cell. Ag is the front electrode. The SiNx thin film deposited by PECVD on the frontside is served as the antireflection layer [6,7] and passivated layer [7–9]. As the antireflection layer, the refractive index and thickness need to be controlled in order to have destructive interference for the reflected light and then increase the light absorption. As the passivated layers, SiNx bonds the surface of Si to decrease the number of dangling bonds on the Si surface, which can reduce the trapping of

the minority carriers by the dangling bonds. If the minority carriers get trapped, they are easy to be recombined and can not output the power. The roughness on the frontside created by wet etch can increase the trapping of sunlight [10]. The P-doped n^+ Si and B-doped p Si base which is solar grade Si form the p-n junction to drive the electrons and holes excited by sunlight. On the backside, there are Al back contact, Al-Si alloy and Al-doped p^+ Si formed from the reaction between the Al paste and p Si base by the high-temperature firing.

There are different kinds of solar technologies including c-Si solar cells, thin film Si solar cells and solar cells made by compound semiconductors such as GaAs and CdTe. Since c-Si is an indirect bandgap material, the absorption ability of sunlight is poor. As a result, the thickness of c-Si solar cells is thicker than other solar cells made from direct bandgap materials such as CdTe in order to increase the sunlight absorption. The typical thickness of the c-Si solar cell is ~180-200 μm.

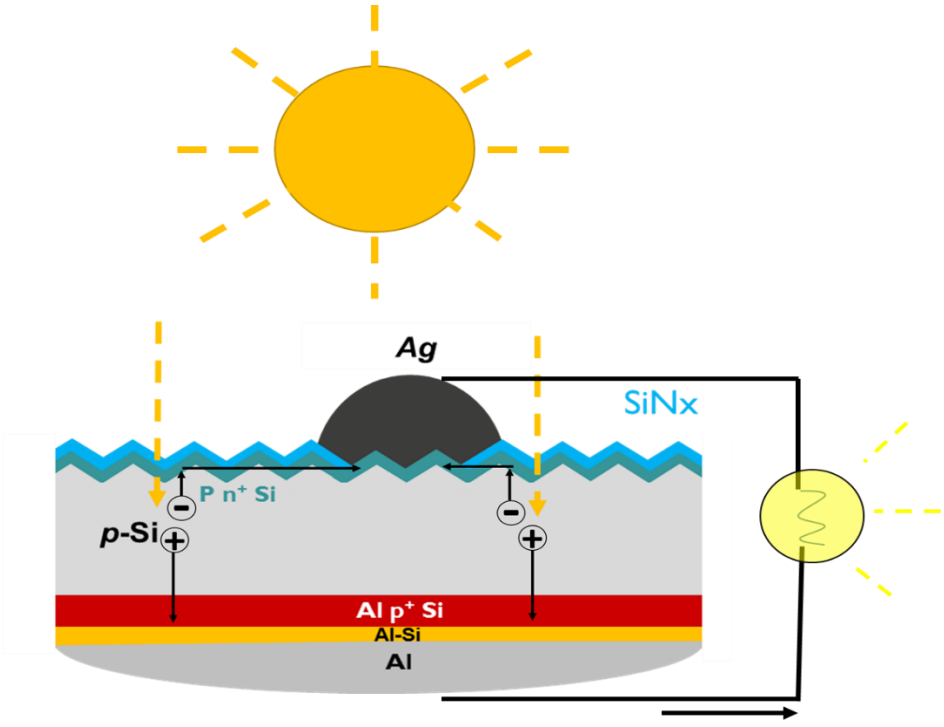

Fig. 1.2 Schematic of the working principle for a c-Si solar cell.

The c-Si solar module is formed by c-Si solar cells connected by interconnected wires, packaged by EVA (ethylene vinyl acetate) films, backsheets (polyvinyl fluoride), glasses, Al frames and junction boxes…etc. Commercially, there are 60-cell modules and 72-cell modules. The average power for a 60-cell module is about 250 Wp. Fig. 1.3(a) shows the top view of a c-Si solar cell and Fig. 1.3(b) represents the installation from cells to a module.

(a)

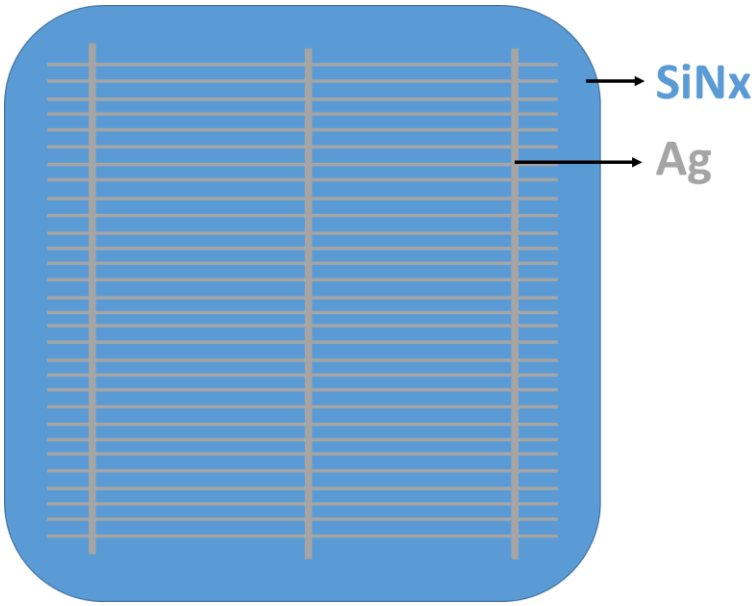

(b)

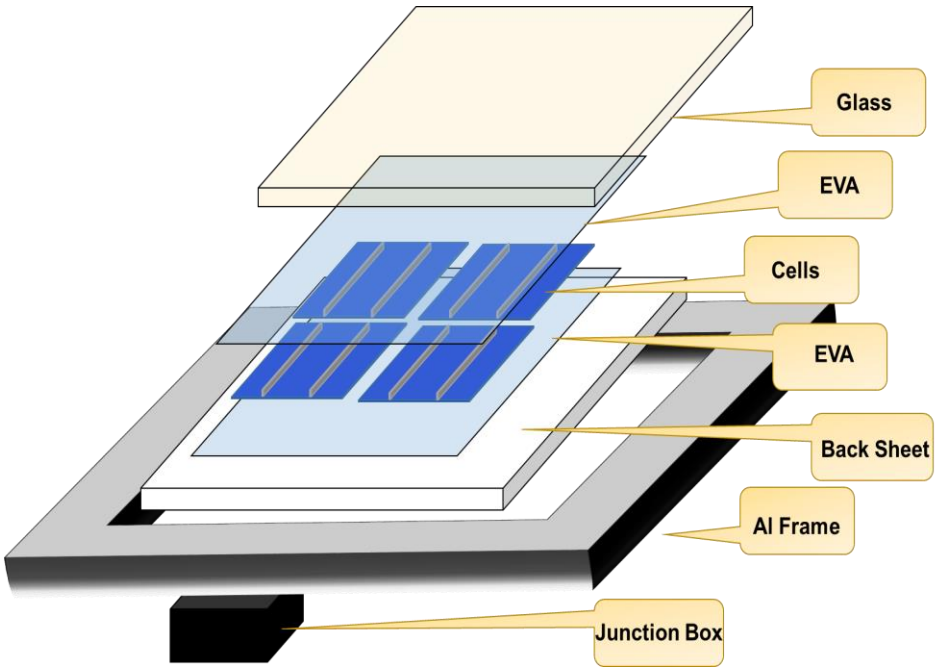

Fig. 1.3 Topview of a c-Si solar cell (a) the composition of a c-Si solar module (b).

From Fig. 1.2, the thickness of a c-Si solar cell is 180–200 μm thick. The P doped n^+ Si which is front emitter is ~0.5 μm thick. The Al-doped p^+ Si which is a back surface field (BSF) is ~10 μm thick. The SiN_x antireflection layer is 75 nm thick. The front electrode is Ag and the back electrode Al. In a module, the cells are interconnected by soldering Cu wires onto them. The solder is made of Sn and Pb. The interconnected cells, two sheets of ethylene vinyl acetate (EVA) and a backsheet of polyvinyl fluoride (PVF) are laminated to the front glass. An Al frame seals the edges of the module. A junction box is attached to the backside of the module for electrical connection.

1.3 Previous Works on Recycling Crystalline-Si Solar Modules

Recycling is rarely practiced for Si modules. As of today, only the European Union enforces solar module recycling. An organization, PV CYCLE, manages module recycling in Europe. The technology practiced by PV CYCLE for Si module recycling involves first stripping the Al frame and junction box from a module and then shredding the remaining module for glass [11]. Si modules have a complex structure (Fig. 1.3(b)). As a rule of thumb, shredding or milling Si modules does not effectively separate the various materials in them [12,13]. To finance PV CYCLE's operation, the European Union imposes a fee on module manufacturers. This fee is ultimately passed onto consumers.

Three approaches have been reported to recycle the Si cells from the modules. Before 2005, the focus was on recovering the cells from the modules and then reusing the reclaimed cells in new modules. The key for this approach is a gentle method to separate the cells from the modules, so the cells remain intact. After the removal of the Al frame and junction box by mechanical measures, the backsheet can be peeled off [14]. There are three methods to detach the cells from the glass. The first method is to dissolve EVA in HNO_3 [14]. This is a long process taking ~24 hrs, and HNO_3 damages cell components including the Ag and Al electrodes. The second method is to dissolve EVA in an organic solvent [15]. A large number of organic solvents have been screened, and the process is really slow taking weeks. The process can be sped up with ultrasonic agitation [16], but the cost and energy input for the ultrasonic process are likely high. The third method is to thermally decompose EVA [17–20]. It can be carried out in a quartz-tube furnace, conveyor-belt furnace or fluidized-bed furnace in air or N_2. The exothermic reaction of burning EVA serves as a heat source for the furnace [19], reducing the energy input for the

furnace. Since the reclaimed cells often suffer from damage [19], the second approach is to reclaim the Si wafers from the modules. New cells are then fabricated on the reclaimed wafers. Reclaiming wafers requires the removal of the Ag and Al electrodes, SiN_x layer, emitter and back-surface field [19][21–24]. The chemicals for this purpose include HF for SiN_x and Al, HNO_3 for Ag, NaOH for Si, a mixture of HF and HNO_3 for Si and SiN_x, KOH for Al, or H_3PO_4 for Al.

Since 2005, the thickness of the wafers has been reduced to 180–200 μm. The thin wafers prevent cell or wafer reclamation since the cells will all break during separation from the glass [25]. Therefore, the most recent approach focuses on recovering the solar-grade Si from the cells [23][26][27]. On the other hand, few papers have discussed metal recovery from Si modules [28]. Two papers mentioned Ag recovery from Si cells by dissolving it in HNO_3 and extracting it through electrowinning [22][27], but the Ag electrode in Si modules is actually covered under soldered Cu. There has been no report on the recovery of multiple metals from Si modules.

In this thesis, recent progress in c-Si module recycling is reported. The objective is to develop a recycling technology for Si modules that is technically, environmentally and financially sustainable. It involves a multi-step process to break down Si modules and recover various materials including all the toxic and valuable materials, solar-grade Si, Ag, Pb, Cu and Sn. The process recovers over 95% of the module by weight. The chemicals for recycling are carefully chosen so their wastes have a minimal environmental impact. More importantly, this recycling process generates a revenue stream of over $12/module from the recovered solar-grade Si and Ag, which is more than enough to cover the cost of recycling.

1.4 Chapter Outline

In the chapter, the background why c-Si solar modules should be recycled is introduced. Since their huge market share and lifetime, the recycling process needs to be developed to achieve sustainable solar energy. Several works regarding the recycling process are also discussed in the chapter.

In Chapter 2, the profit for recycling c-Si solar modules is analyzed, which is an important factor of incentives as a business. The Ag and solar grade Si are the target materials for recycling due to their high value and energy cost, respectively. The network of collecting c-Si solar modules is also suggested to reduce the cost of collection.

In Chapter 3, the proposed recycling process for c-Si solar modules is described. It includes the breakdown of modules, metal recycling and solar grade Si recycling. First, the breakdown of the modules contains Al frames and junction boxes recycling, EVA burning and the separation of the interconnected cells. Second, the metals on the interconnected cells are leached by the solution and then recovered by electrowinning. Then the heavily doped Si parts of the cells are removed to recover solar grade Si.

In Chapter 4, the equipments used for the proposed recycling process including the 4-point probe, scanning electron microscope (SEM) and electrochemical capacitance-voltage profiler (ECV) are introduced.

In Chapter 5, the experimental part of the metal recycling from c-Si solar modules is reported. The metals are leached by the optimized solution and then recovered by sequential electrowinning. The Ag and Cu are successfully recovered with the high purity and recovery rate. The challenge about further improving the recovery rate and the stability of the materials of the electrode is discussed.

In Chapter 6, the solar grade Si recovered from c-Si solar cells is reported. The wet etch process is optimized to remove the heavily doped Si to recover the solar grade Si. The 4-point probe technique is developed to monitor the etch process to recover the maximum amount of solar grade Si. SEM and ECV are used to verify whether the heavily doped Si is removed completely.

CHAPTER 2

INCENTIVES TO RECYCLE CRYSTALLINE-Si MODULES

2.1 What to Recycle?

There are two valuable materials which should be recovered from the c-Si cell in Fig. 1.2, solar-grade Si (p-Si base) and Ag.

The availability of Ag is limited. The worldwide known reserve of Ag is ~530,000 tonnes [29]. At the current mining rate of 26,100 tonnes/year, the Ag reserve would be depleted in 20 years. Recovering Ag from waste Si modules is mandatory to sustain the current solar industry. There are also significant energy savings by recovering solar grade Si from waste Si modules. One of the most energy-intensive steps in the production of c-Si modules is the Siemens process, which reduces $SiHCl_3$ to solar-grade Si [30][31]. Recovering solar grade Si from Si modules bypasses the Siemens process. It is suggested that the energy input to produce a c-Si module is 400 kWh with freshly-produced Si, but only 186 kWh with recycled solar grade Si [32]. This is a ~55% energy saving.

The SiN_x layer and Al back electrode are hard to recover. For the Si wafer in c-Si solar cells, the front emitter and back-surface field are heavily doped. They are out of the specifications for solar-grade Si. Only the base can be recovered as solar-grade Si, which is boron doped to $\sim 1\times10^{16}$ cm^{-3}. Once the cells are soldered to modules (Fig. 1.2), there are three more metals to consider, Pb and Sn from the solder and Cu from the wires. While Sn and Cu may have enough values to recover, Pb is a toxic metal and should be removed from the recycling sludge [33][34]. Besides the valuable and toxic materials, the Al frame, junction box, front glass and polymer sheets (EVA and PVF) should be recycled as well.

These components have little values as raw materials [35], but their recovery is environmentally sound.

2.2 Revenue from Crystalline-Si Modules Recycle

A typical 60-cell Si module contains ~0.65 kg of Si. If 85% of the Si is recovered as solar-grade Si, it is worth $8.20/module at $15/kg for solar-grade Si. The module also contains ~6.5 g of Ag. If 95% of the Ag is recovered, it is another $4.30/module at $20/oz for Ag. As a result, the valuable materials in a typical Si module add to over $12, which is more than enough to cover the cost of recycling for a profitable recycling business without any government support. The estimation is much higher than the analysis by the International Renewable Energy Agency, which predicts $15 billion in revenue from recycling 78 million tonnes of solar modules. The estimation is ~$45 billion from 78 million tonnes of solar modules. This is because the process in the thesis keeps high-value materials in their pure, high-value forms.

2.3 Network for Collecting Solar Modules

A major contributor to the cost of solar module recycling is the cost to collect and transport solar modules which are scattered around in small quantities [35]. To contain the collection cost, we propose to utilize the current distribution network of solar modules in the reverse order as a collection network (Fig. 2.1). Installers go to homes to perform repair and pick up waste modules. The waste modules are shipped to retailers, then to distributors and finally to recyclers who operate centralized recycling plants and generate revenues by selling the recovered solar-grade Si and Ag to the solar industry. To finance the network, each party in this collection network receives monetary compensation from the next party in the value chain.

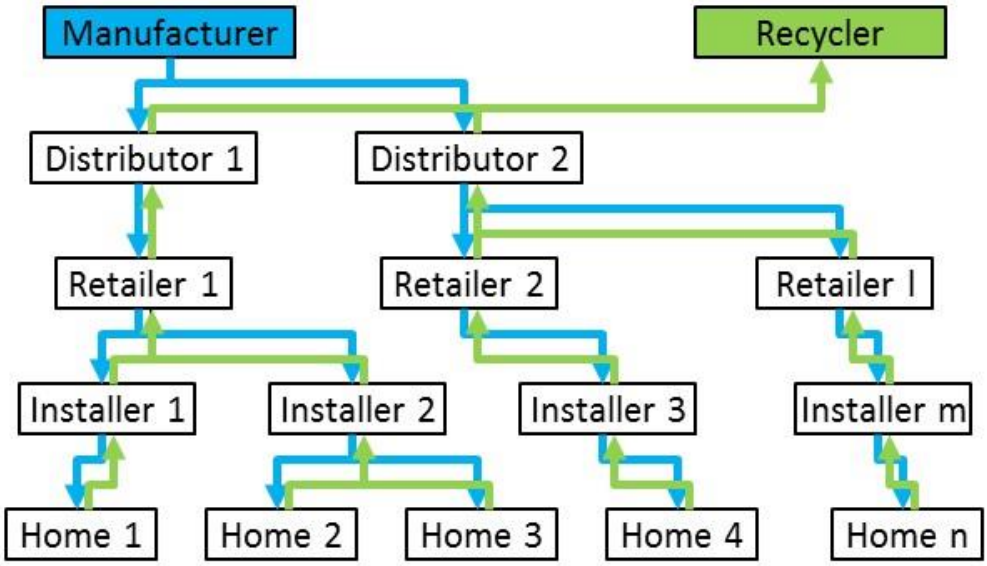

Fig. 2.1 A collection network for solar module recycling based on the current distribution network.

CHAPTER 3

PROPOSED PROCESS TO RECYCLE CRYSTALLINE-Si MODULES

3.1 Overview of Proposed Process to Recycle Crystalline-Si Solar Modules

Fig. 3.1 is the proposed process to break down c-Si modules and recover various materials. It involves three steps, module recycling, cell recycling and waste handling. In the first step, the junction box and Al frame are mechanically removed from a module. The polymer sheets (EVA and PVF) are then burned off to separate the cells from the glass in a furnace [36], which serve as a heat source for the furnace. This is different from the report on peeling off the PVF [14], as PVF wastes can be either burned or buried. The glass is recycled and what is left is a string of interconnected cells. In cell recycling, interconnected cells are first immersed into a leaching solution to dissolve four metals, Ag, Pb, Cu and Sn. These metals are then recovered from the leaching solution one by one through electrowinning. The remaining cells are immersed into an etching solution to remove the SiN_x layer and Al back electrode. Finally the cells are immersed into another etching solution to remove the emitter and back-surface field and to recover the base as solar-grade Si. The remaining sludge goes to landfill.

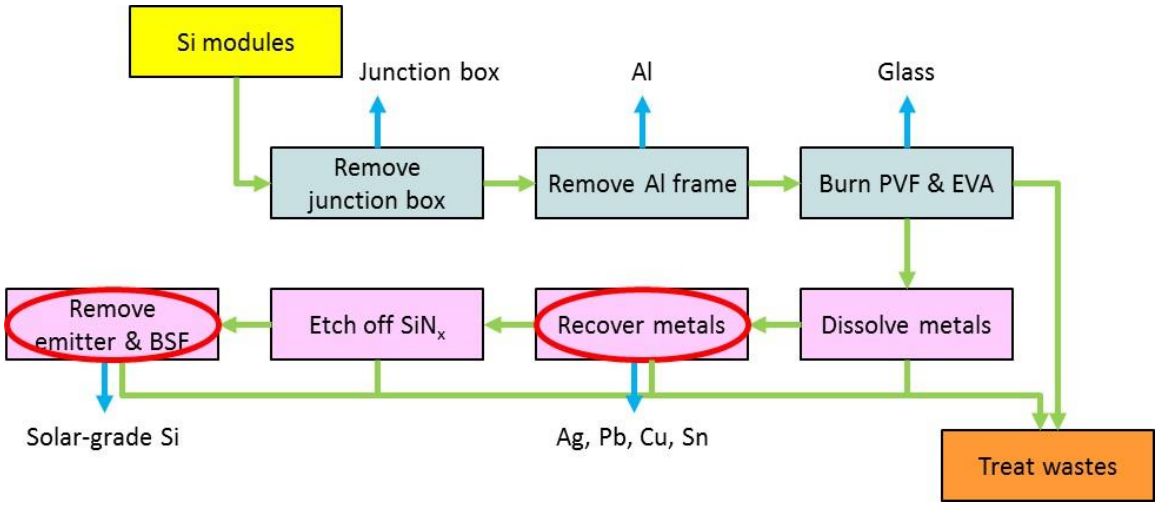

Fig. 3.1 A proposed process to break down c-Si solar modules and recover various materials.

The chemicals selected for cell recycling are critical as they determine the waste chemicals people have to deal with. On the other hand, it is desirable to employ selective, self-limited chemistries for cell recycling (Fig. 3.2). We have purposely chosen HNO_3 which dissolves only Ag, Pb, Sn and Cu from the cells (Fig. 3.2(b)), and HF which etches only Al, Al-Si alloy and SiN_x on the cells (Fig. 3.2(c)). With self-limited chemistry, process control becomes simpler as there is no over-etch to worry about. Finally NaOH is used to remove emitter and back-surface field (Fig. 3.2(d)). This is not a self-limited process, so a method to monitor the Si etch process is needed to maximize the amount of solar-grade Si recovered.

The last step is waste handling. Our recycling process generates three waste solutions, NaOH, HNO_3 and HF. NaOH and HNO_3 can neutralize each other to form a solution of $NaNO_3$, which is a fertilizer [37]. There is a well-established practice to treat HF wastes, i.e. $Ca(OH)_2$ is added to HF to precipitate fluorine out as CaF_2 [38]. There are also two gaseous exhausts from the recycling process. One is the exhaust from the polymer-burning

furnace, which contains fluorine. The other is the exhaust from metal dissolution in HNO_3, which contains NO and/or NO_2. Scrubbers are required to trap fluorine in water as HF and to trap NO and NO_2 in water as HNO_3. It is possible to use the acids from the scrubbers in the recycling process.

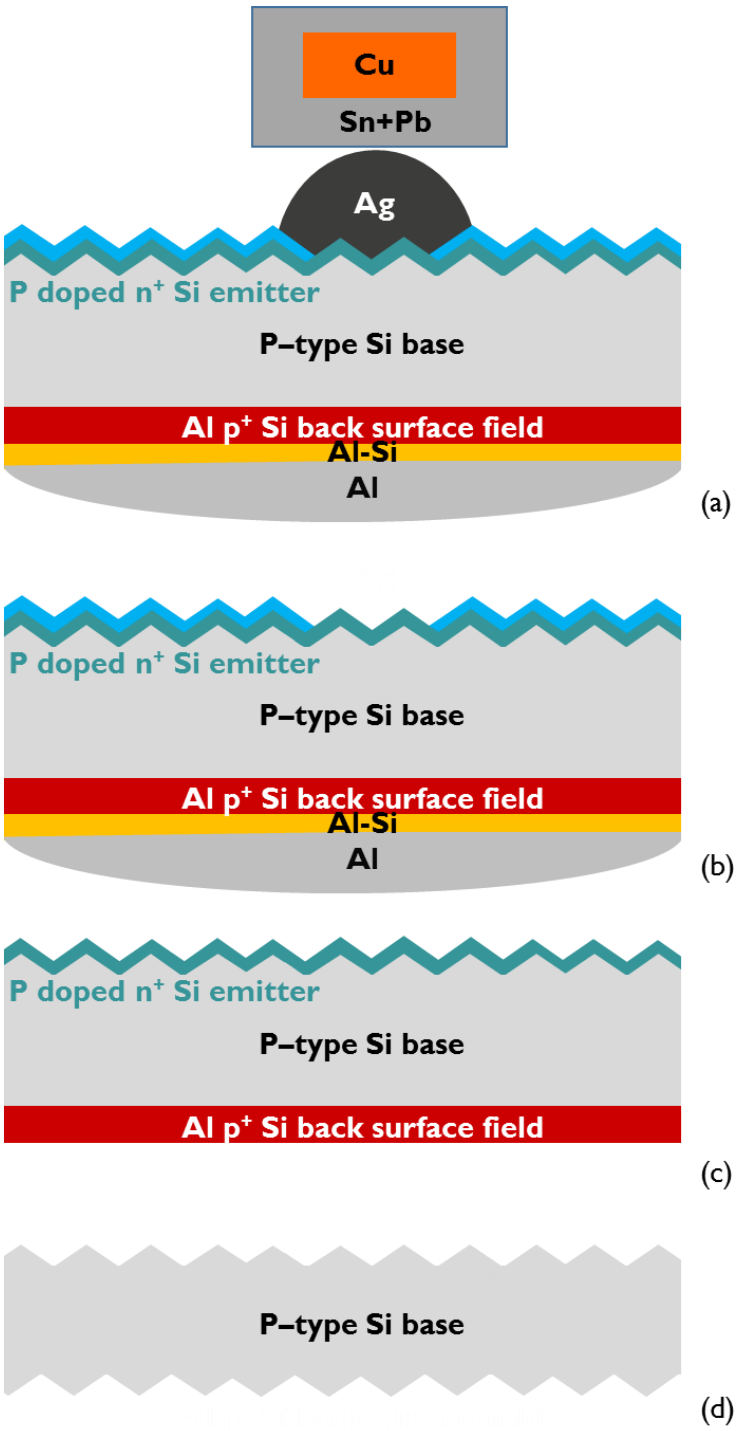

Fig. 3.2 Self-limited chemistries for cell recycling: before HNO_3 (a); after HNO_3 (b); after HF (c) and after NaOH (d).

It is estimated that over 95% of the module by weight can be recovered through our recycling process, as it can recover all the glass, Al frame, junction box, polymers (as heat source), 85–90% of the Si and 90–95% of the metals. On top of 95% recovery, this process can generate over $12/module in revenue by selling the recovered solar-grade Si and Ag to the solar industry.

For the proposed recycling process in Fig. 3.1, the technologies for module recycling and waste handling have been more or less developed or at least explored. However, the technology for cell recycling is not ready yet. In particular, the technology to recover multiple metals from Si modules and the technology to maximize the amount of solar-grade Si recovered need to be developed, which are circled in Fig. 3.1. In the next chapters, multiple metals recovery by electrowinning [28] and solar-grade Si recovery by wet etch [26] will be reported.

3.2 Techniques Introduction for Recycle

The techniques used for metals and solar grade Si recycle are electrowinning and wet etch.

Electrowinning

Electrowinning is the process which extracts pure metals from impure metals. Impure metal is leached by the solution. Energy is applied via voltage source to reduce metal ions from the solution. Cu is one of the metals recovered by the electrowinning in the industry [39–43]. When the applied voltage reaches the certain value to reduce the certain metal, the applied voltage is the minimal energy to reduce the metal ion which is called the reduction potential. The reduction potential of a material is affected by the material

property and activity of the material. Nernst equation describes the relationship between equilibrium reduction potentials and the activities with different materials:

$$E_{red} = E^0 + \frac{RT}{nF} ln(a_M) \quad (3.1)$$

where E_{red} is the reduction potential under nonstandard conditions, E° the standard reduction potential (reduction potential under 298 K, 1 atm and 1 M solution), R the gas constant, T the absolute temperature, n the number of electron involved in the reaction, F the Faraday constant and a_M the activity of the metal ion. For the dilute aqueous solution, the activity of the metal ion is equal to the concentration of the metal ion. The reduction potentials of different metals leached from c-Si solar modules can be determined by Nernst equation. After determining the reduction potential for each metal, the voltage can be applied to recover the metals.

Wet Etch

Wet etch has several advantages for the c-Si solar modules recycle. It does not need expensive equipment such as dry etch and can process huge amounts of solar modules fast. Wet etch has the very high selectivity between different materials. In the recycle process, HNO_3 is used for metal dissolution and does not affect SiNx and Si. HF only removes SiNx. NaOH is then used for the heavily doped Si removal. Due to high selectivity between different materials, the wet etch can be a self-limited process to precisely remove the desired materials without monitoring. However, for the heavily-doped Si removal, the process needs to be monitored to control the etch time since NaOH does not have the selectivity between heavily doped Si and solar grade Si. A 4-point probe is used to measure the sheet resistance to monitor the etch process in order to control etch time to recover the maximum amount of the solar grade Si.

CHAPTER 4

INTRODUCTION OF EQUIPMENTS FOR RECYCLE

4.1 4-point Probe

The 4-point probe is used for measuring the resistance of semiconductors. It can measure bulks or thin films. Fig. 4.1 is the illustration of the 4-point probe. The principle of the 4-point probe is that the 4 probes inserted into the material and then the current flows from the first probe to the measured material and then to the fourth probe. The second probe and third probe are connected to the voltmeter to measure the voltage drop and only trace amount of the current flows to the second and third probes due to the high resistance of the voltmeter.

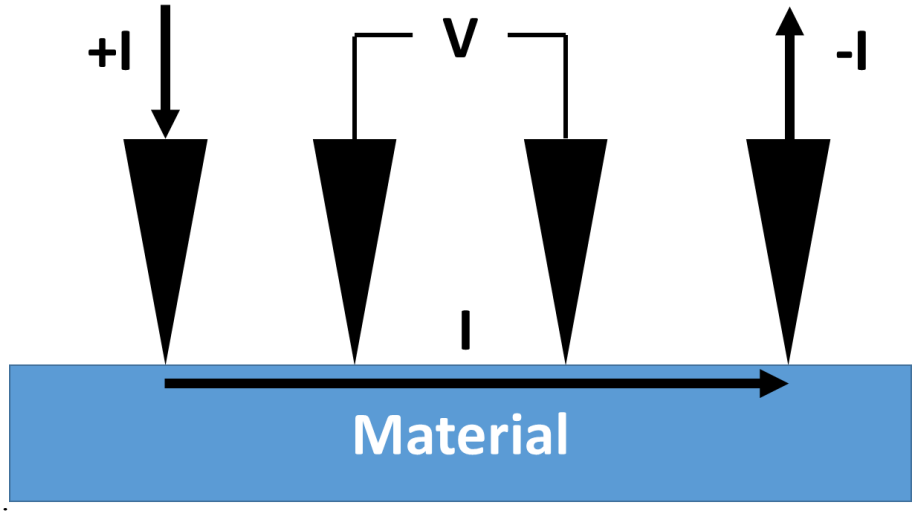

Fig. 4.1 Schematic of 4-point probe

Fig. 4.2 is the circuit diagram of a material measured by a 4-point probe. By separating the voltage measurement and applied current, the voltage drop measured by the voltmeter is only caused by $R_{material}$ due to almost no current flowing into the voltmeter. As a result,

the resistance by the measurement can be assumed as $R_{material}$ by dividing the voltage measured with the current applied.

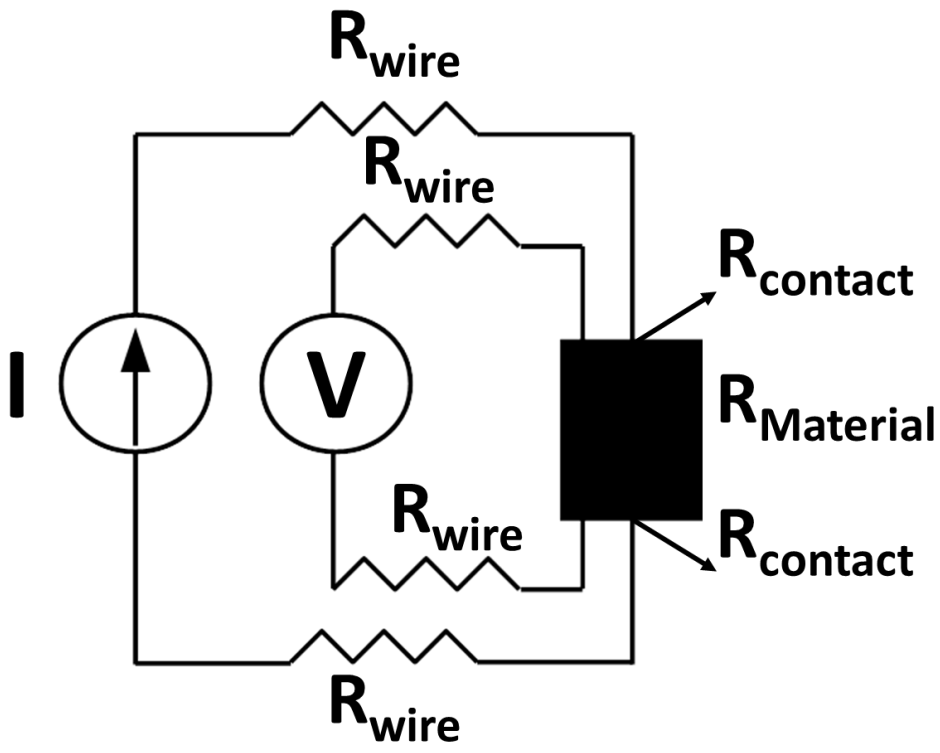

Fig. 4.2 Circuit diagram for a 4-point probe measurement.

However, if only two probes are used for the resistance measurement as Fig. 4.3, the voltage drop is caused by $R_{material}$, $R_{contact}$ and R_{wire}. The measuring resistance has a larger deviation from the $R_{material}$ by dividing the voltage measured by the applied current.

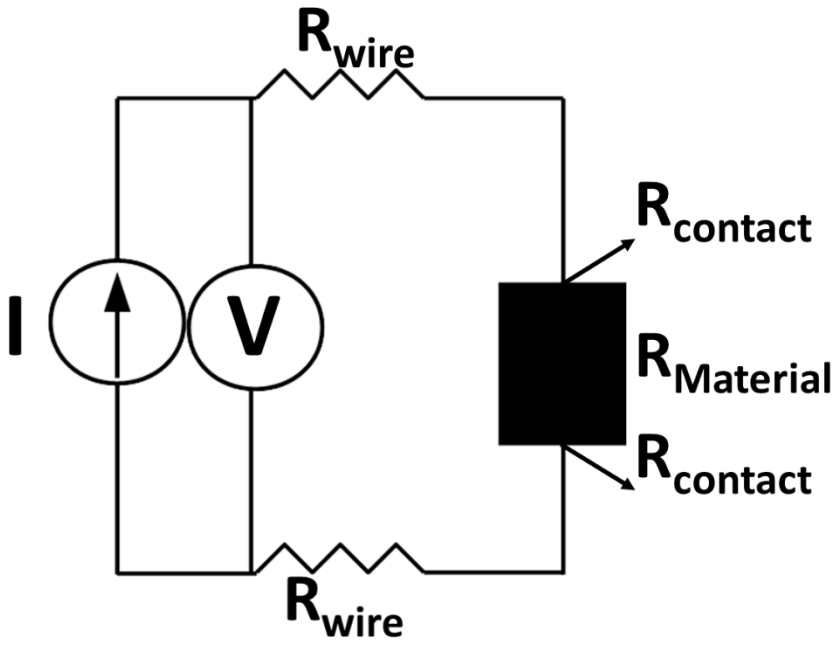

Fig. 4.3 Circuit diagram for a 2-point measurement.

Depending on different thicknesses of material, the 4-point probe can measure its resistivity and sheet resistance by measuring the resistance. Fig 4.4 uses spreading current to explain how to measure the resistivity and sheet resistance of a material. The thickness of the material is t and the spacing between probes is d. Assuming t > 0.5d. The current spreads into material spherically. The radius of the spreading current is r. The voltage at the second probe is shown as:

$$\boldsymbol{V_2 = IR = I \times \rho \frac{L}{A} = -I \int_{2d}^{d} \frac{\rho dr}{2\pi r^2} = \frac{I\rho}{2\pi} \times \frac{1}{2d}} \quad (4.1)$$

The voltage at the third probe is:

$$\boldsymbol{V_3 = -I \int_{d}^{2d} \frac{\rho dr}{2\pi r^2} = -\frac{I\rho}{2\pi} \times \frac{1}{2d}} \quad (4.2)$$

where ρ is the resistivity of the material, A the cross-section area which the current flows through, L the length which the current flows through The voltage between the second and the third probe is then as follows:

$$\Delta V_{23} = \frac{I\rho}{2\pi d} \quad (4.3)$$

According to the applied current and the measured voltage, the resistivity can be calculated as:

$$\rho = 2\pi d \frac{\Delta V_{23}}{I} \quad (4.4)$$

This is the resistivity measurement for a bulk material with the thickness t > half of the probe spacing d. However, for a thin film material, the thickness t < half of the probe spacing d. The voltage at the second probe can be rewritten as follows:

$$V_2 = I \times \rho \frac{L}{A} = -I \int_{2d}^{d} \frac{\rho dr}{2\pi rt} \quad (4.5)$$

where $2\pi rt$ replaces $2\pi r^2$. Then the voltage difference between the second and third probe is:

$$\Delta V_{23} = \frac{I\rho}{\pi t} ln2 \quad (4.6)$$

From the equation, the sheet resistance can be measured as follows:

$$\frac{\rho}{t} = \frac{\pi \times \Delta V_{23}}{ln2 \times I} \quad (4.7)$$

As a result, for a thin film material, the sheet resistance can be measured by the 4-point probe.

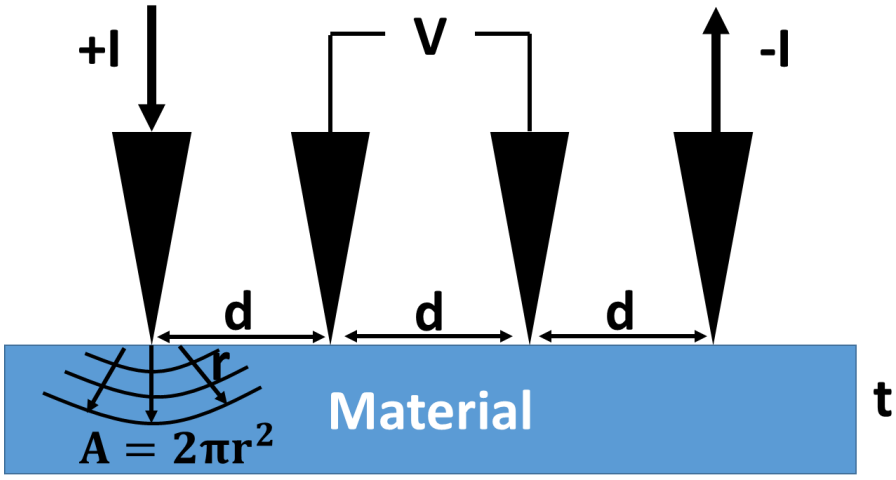

Fig. 4.4 Schematic of the spreading current from a 4-point probe

In this research, 4-point probe is used for measuring c-Si solar cells. The average thickness of c-Si solar cells is about 180-200 μm. The probe spacing is about 0.5-1 mm. As a result, the sheet resistance is measured from c-Si solar cells by the 4-point probe.

4.2 Scanning Electron Microscope (SEM)

Scanning electron microscope (SEM) is a characterization tool for microstructures of materials. The electron gun emits the electron beam to scan the surface of the materials. The interaction between the electron beam and the atoms in the material creates a lot of signals. The signals can be detected by their specific detectors, which reveals the information of the materials such as topography, morphology, chemical composition, crystallographic information.

The electron beam is generated by the electron gun and then focused on the specimen by the magnetic lens. Fig. 4.5 shows the signals which are generated from the material by the incident electron beam.

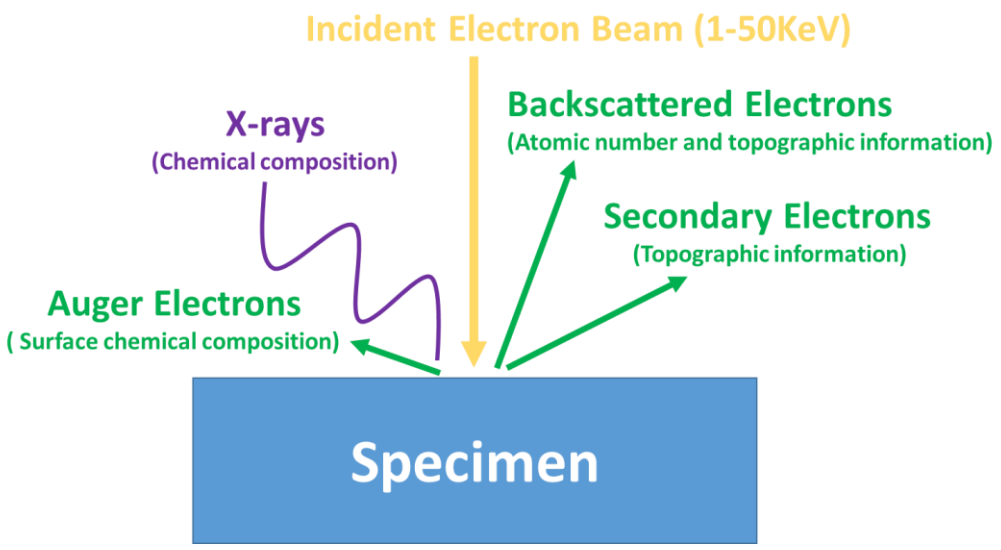

Fig. 4.5 Signals from the specimen interacted with electron beams in SEM

Backscattered electron (BSE)

Backscattered electron (BSE) is produced from the elastic interaction between beam electrons and nuclei in an atom of the specimen and they have high energy and the large escape depth. BSE is sensitive to the atomic number (Z). The BSE yield is proportional to Z. If there is the region on the specimen with higher Z, the BSE image will show brighter in the region. As a result, BSE image can show Z contrast for the specimen.

Secondary electron (SE)

Secondary electron (SE) is produced by inelastic interactions of beam electrons with electrons in the valence or conduction band of atoms in the specimen, resulting in the ejection of the electrons from the atoms. These ejected electrons are termed secondary electrons. Typically the energy of secondary electrons is less than 50 eV. SE yield is independent of Z and decreases with increasing incident beam energy and increases with decreasing the grazing angle of the incident beam.

SE production is very sensitive to the topography. The contrast of the topography can be produced by SE. SE has very low energy, which results in their small escape depth. Only SE produced near the surface can be detected.

Auger electron

The incident beam electrons cause ionization of atoms. Subsequent relaxation of the ionized atoms causes the emission of Auger electrons revealing the characteristic of the elements presenting in this part of the sample surface. As a result, Auger electrons can provide the chemical composition information on the surface of the specimen as the escape depth of Auger electrons is very small (~few nm).

Energy dispersion spectrometer (EDS)

Energy dispersion spectrometer (EDS) uses the X-rays generated from the specimen to characterize the chemical composition of the specimen. The X-rays are produced by the interaction between the incident electron beam and the electrons of the atoms in the specimen. When the electrons in the inner shells are emitted by the incident beam electrons, the vacancies in the inner shells are filled by the electrons from the outer shells, which will generate the X-rays. The energy of the X-rays is the energy difference between outer-shell electrons and inner-shell electrons. Since the energy difference between shells is the characteristic for individual elements, the X-rays are called characteristic X-rays. Thus, characteristic X-rays are used for chemical composition characterization. Fig. 4.6 is the illustration for the generation of characteristic X-rays. The characteristic X-rays which are generated from K shell are called K lines. If the characteristic X-rays are generated from L and M, they are called L lines and M lines, respectively. Furthermore, if the incident

electrons are decelerated by atomic nuclei, the different X-rays without atom information are generated. These X-rays are called continuous X-rays.

The energy dispersion spectrometer (EDS) is used to analyze the characteristic X-rays from the specimen. The characteristic X-rays with certain energy emit into the semiconductor detector and then generated the electron-hole pairs. The process of X-rays detection then becomes measuring the number of free charge carriers (electrons and holes) created in the crystal during the absorption of each X-rays. By separating each X-rays photon and measuring the amount of current produced by each X-ray photon to determine its energy, the intensity versus different energy of X-rays can be found. From the intensity and energy of X-rays, the concentration and the species of atoms can be determined, respectively. Typically, the detection limit of EDS is about 1%.

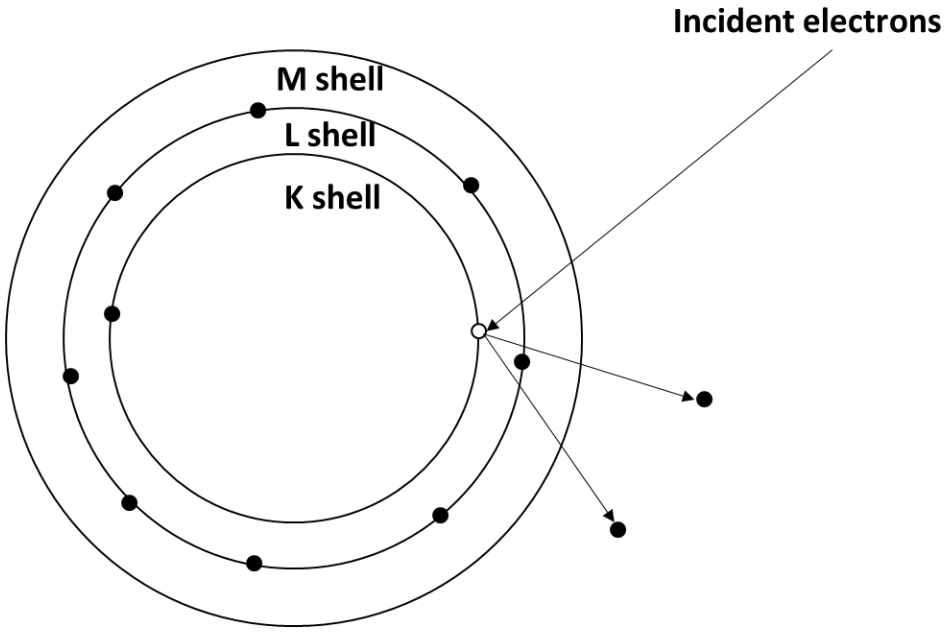

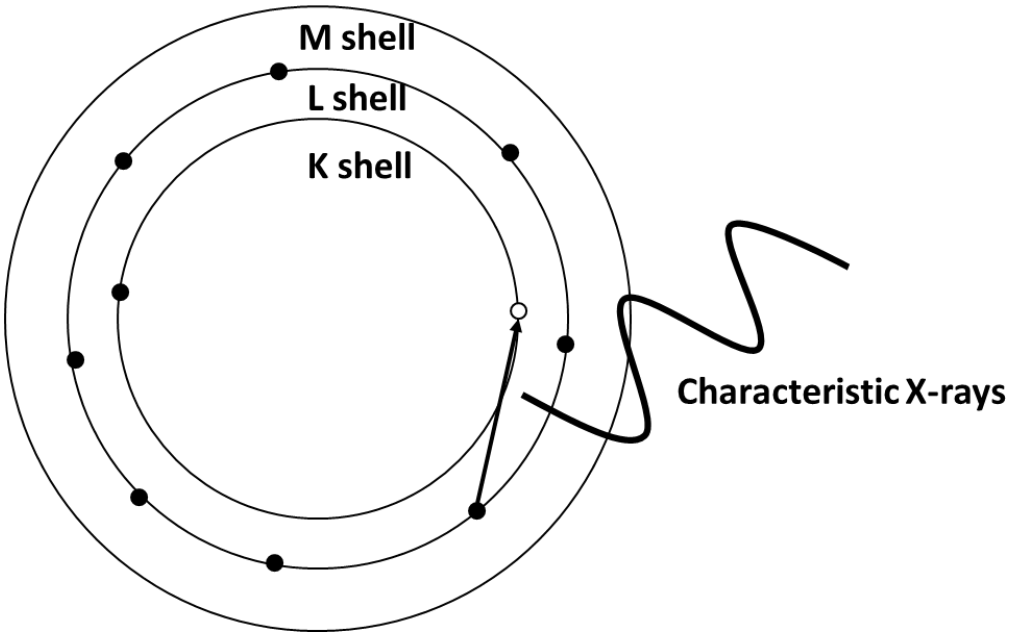

Fig. 4.6 The Generation of characteristic X-rays by SEM.

These are the signals which are usually detected by SEM. These signals represent the information from different depths in the specimen since they have different escape depths. Fig. 4.7 is the spatial resolution of signals from the interaction between the electron beam and the specimen. The Auger electrons are generated from the depth < 1 nm so the information of that is highly surface sensitive. Then the secondary electrons originate from about 10 nm depth and 10 nm lateral radius. Backscattered electrons are created from 1 μm depth and 1 μm lateral radius, and the X-rays have about 5 μm in both depth and lateral radius.

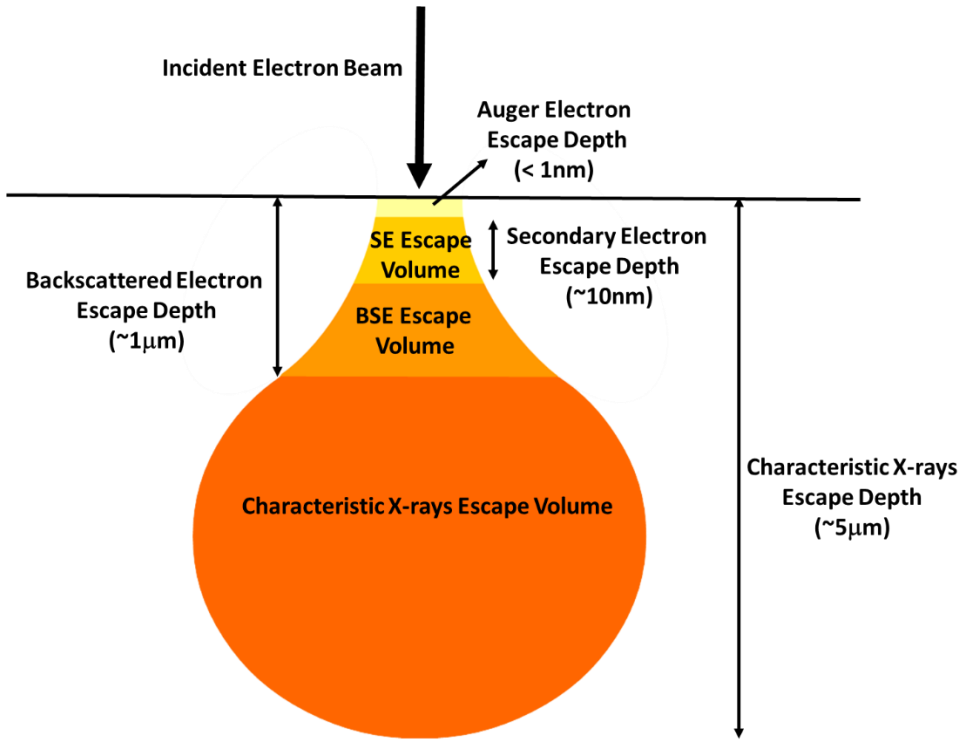

Fig. 4.7 The spatial resolution of the signals by SEM

4.3 Electrochemical Capacitance-Voltage (ECV)

The Electrochemical Capacitance-Voltage (ECV) profiling technique is used to measure the active carrier concentration profiles in semiconductor layers.

The technique uses an electrolyte-semiconductor Schottky contact to create a depletion region, a region which is without electrons and holes, but contains ionized donors. The depletion region with its ionized charges inside behaves like a capacitor. The measurement of the capacitance provides information of the doping and electrically active defect densities. Depth profiling is characterized by practicing both electrolytically etching the semiconductor and the capacitance measurements. The next section will introduce the principle of capacitance measurement for carrier density.

Capacitance-Voltage (C-V)

The principle of carrier density characterization by the capacitance-voltage method is from the depletion region as a capacitor by applying a DC voltage. Fig. 4.8 is a p-type semiconductor. In order to create the depletion region, the DC positive voltage V needs to be applied on the metal deposited on the p-type Si in order to deplete majority carriers in the p-type Si and then the depletion region is created. The AC voltage ν is used to measure the capacitance.

DC voltage V plus an AC voltage ν are used. When the AC voltage increases from zero to a small positive voltage, a charge dQ_m will be added to the metal contact. The charge increment dQ_m must be balanced by an equal semiconductor charge increment dQs for charge neutrality. The semiconductor charge is given:

$$\boldsymbol{Q_s = qA\int_0^W (p - n + N_D^+ - N_A^-)dx} \quad (4.8)$$

where q is a unit charge, A the area of the cross-section of the semiconductor, W the depth of the depletion region, p hole density, n is electron density, N_D donor density and N_A the acceptor density. Since p-type Si is used, N_D and n are almost zero. In the depletion region, p is almost zero. The equation is then as follow:

$$\boldsymbol{Q_s = -qA\int_0^W N_A\, dx} \quad (4.9)$$

The measured capacitance is as follows:

$$\boldsymbol{C = -\frac{dQ_s}{dV} = qA\frac{d}{dV}\int_0^W N_A dx = qAN_A(W)\frac{dW}{dV}} \quad (4.10)$$

The above equation, assuming N_A does not change over dW distance. As a result, $dN_A(W)/dV$ is neglected.

The capacitance of the reversed junction can be considered as the parallel plate capacitors:

$$C = \frac{K_s \varepsilon_0 A}{W} \quad (4.11)$$

where Ks is relative permittivity, ε_0 vacuum permittivity.

Differentiating Eq. (4.11) with respect to voltage and replacing dW/dV into Eq. (4.10) :

$$N_A(W) = -\frac{2}{qK_s \varepsilon_0 A^2 d(1/C^2)/dV} \quad (4.12)$$

W can be calculated from Eq (4.11), C as the voltage can be measured. From the Eq. (4.12), the carrier density at W can be characterized. This is the principle how capacitance-voltage measures the carrier density. With applied different DC voltages, different depths of the depletion region are achieved. The carrier profile can be characterized [44].

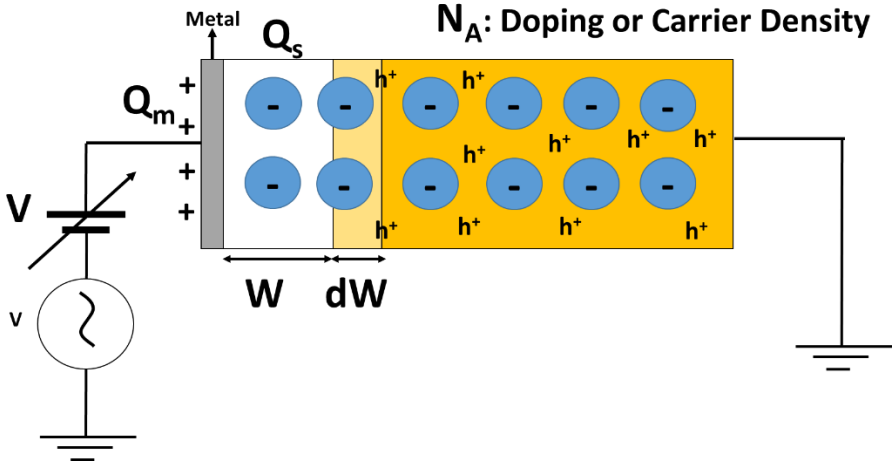

Fig. 4.8 Schematic of Capacitance-Voltage (C-V) measurement.

ECV setup

Fig. 4.9 is the ECV setup. The semiconductor specimen is pressed on a sealing ring in the electrochemical cell with an electrolyte. The area of ring opening defines the contact area of the specimen with the electrolyte. The electrolyte forms a Schottky barrier junction at the semiconductor interface. The depletion region is created in the semiconductor specimen by applying a constant potential between the semiconductor specimen and the platinum electrode measured with the reference saturated calomel electrode. By forming the depletion region, the carrier density at a certain depth can be measured. Then, the etching conditions are controlled by the current circuit between the semiconductor specimen and the counter electrode. The contact area between the electrolyte and the semiconductor specimen is dissolved electrolytically. The etch depth can be calculated by the etch current and then another carrier density with deeper depth can be measured. The carrier profile can be achieved by etching into semiconductor specimen.

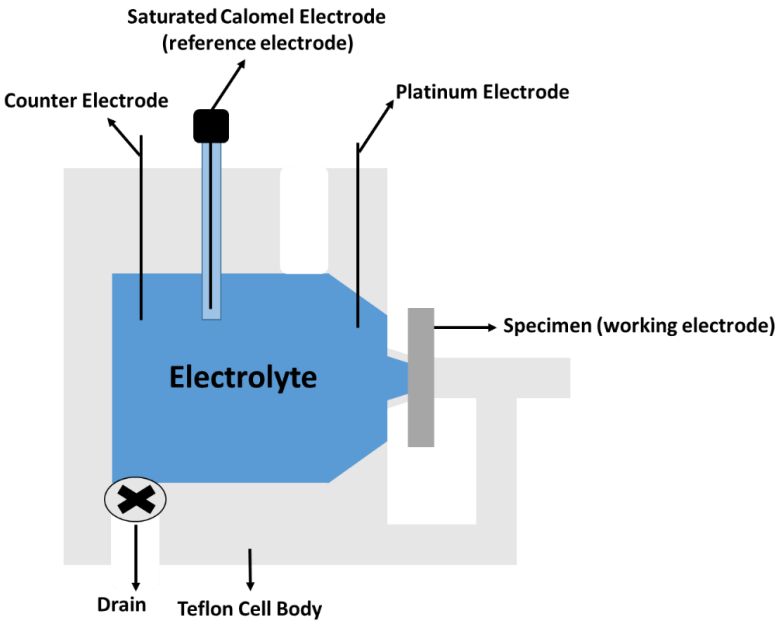

Fig. 4.9 Schematic of ECV profiler setup.

CHAPTER 5

RECYCLE METALS FROM CRYSTALLINE-Si SOLAR MODULES

5.1. Introduction

After module recycling, interconnected cells are separated from the glass. These cells, intact or broken, are first immersed in HNO_3 to dissolve four metals from the cells, Ag, Pb, Sn and Cu. Although there has been no report on recovering multiple metals from Si modules, there are reports on recovering three of the four metals from printed circuit boards by leaching them in HNO_3 [45,46]. Yoo et al. [45] added NaCl to the leaching solution to precipitate Ag out as AgCl. This requires an extra step to convert AgCl to metallic Ag. Mecucci et al. [46] used electrowinning to recover Cu and Pb from the leaching solution. We believe that electrowinning is a more cost-effective approach as it can recover metals in their pure metallic forms. Furthermore, sequential electrowinning can recover multiple metals one by one from the leaching solution.

Fig. 5.1 shows the structure of cells with interconnected wires. Totally, five metals involve in the c-Si solar modules, Ag from front contacts, Al from backcontacts, Cu from interconnected wires, Pb and Sn from solders. HNO_3 is used to dissolve the metals into solution and then the metals are recovered by electrowinning.

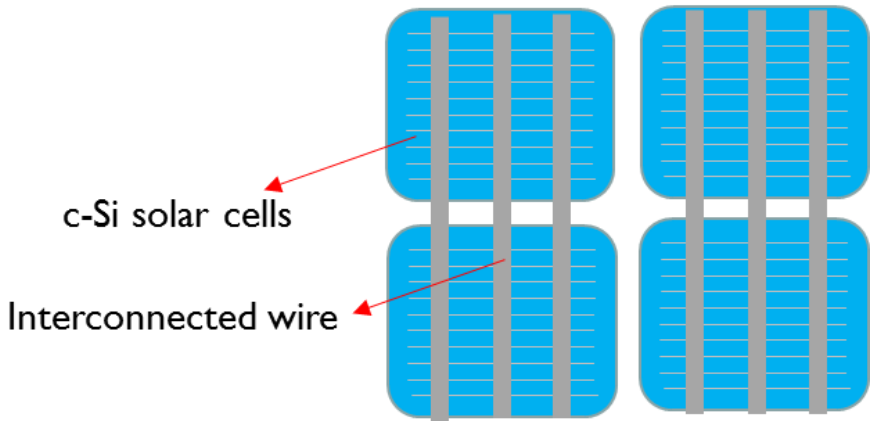

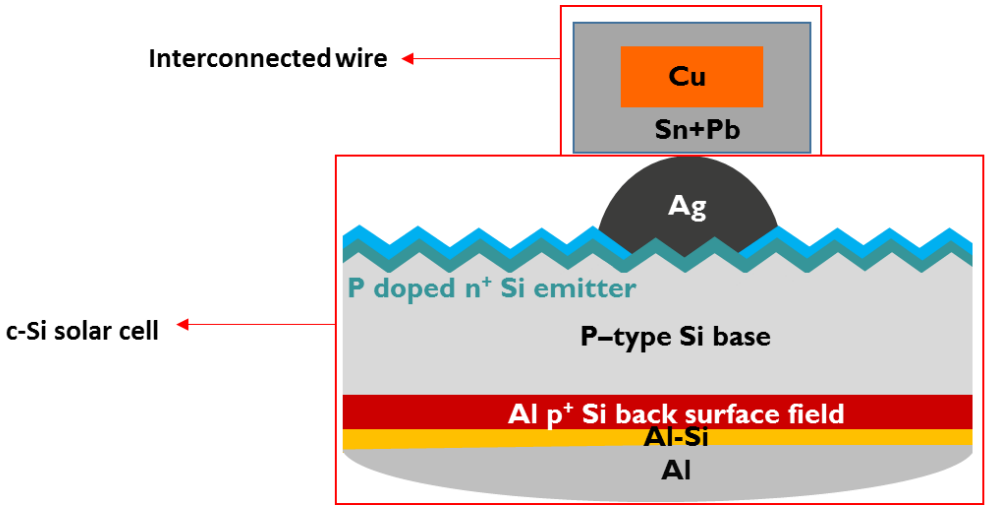

Fig. 5.1 Top view of solar cells with interconnected wires (a) cross section of cells with interconnected wires (b).

5.2 Metal Dissolution from Crystalline-Si Solar Modules

HNO_3 is used to dissolve the metals from c-Si solar modules. HNO_3 can dissolve Ag, Cu, Pb into solution. Sn reacts with HNO_3 to become SnO_2 powder and forms the precipitate. Al can not dissolve into HNO_3 since HNO_3 solution reacts with Al to form a uniform passivated Al_2O_3 film on the Al surface to protect Al. As a result, Al is stable in the HNO_3 solution. Fig. 5.2 shows the flowchart of the metal dissolution. After the process, the SnO_2 precipitate is filtrated from the solution. The final solution will be used for electrowinning to recover the metals.

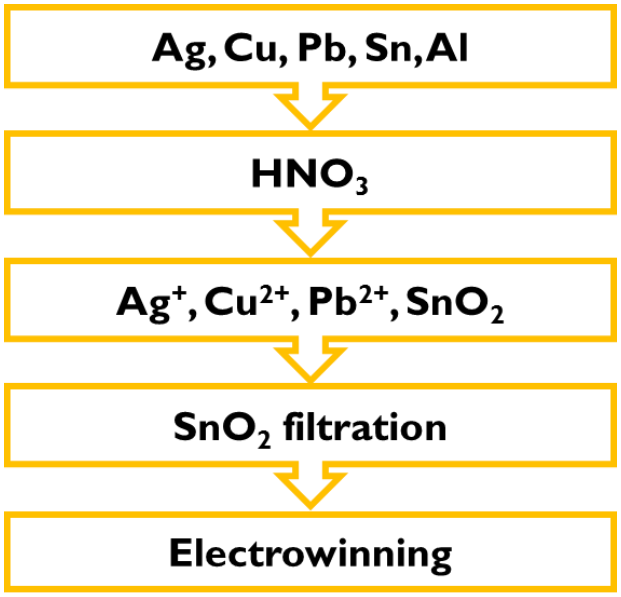

Fig. 5.2 Flow chart of the metal dissolution from c-Si solar modules

During the process, there are three parameters to be controlled. (1) the concentration of the HNO_3 solution (2) the amount of the HNO_3 solution applied (3) temperature.

Concentration of HNO_3 solution

The concentration of HNO_3 affects the dissolution rate in the process. If the concentration of HNO_3 is too low, the dissolution rate of the metals is too low, which will affect the throughput. However, if the concentration of HNO_3 is too high, the reaction is too strong and generates a lot of heat and gas such as NO_2 or NO suddenly, which will cause danger during the process. As a result, controlling the concentration of HNO_3 is necessary.

Amount of HNO_3 solution

The second parameter in the process which needs to be controlled is the amount of HNO_3 solution applied. If the amount of HNO_3 solution is too small, the metals can not be dissolved into the solution completely. Table I shows the weight percentage of each metal

in c-Si solar modules. The amount of Cu is much larger than that of Ag. During the process, if Cu can not be dissolved completely, the Ag ions in the solution will replace the undissolved Cu and then precipitate on it, which will lower the dissolution of Ag. If the dissolution of Ag is low, the recovery rate for Ag by electrowinning will be lower.

If the amount of HNO_3 is too large, after dissolving all the Ag, Cu and Pb, the final solution will contain a lot of residual HNO_3. When the solution is used for electrowinning, the residual HNO_3 will redissolve the recovered Ag into solution and lower the recovery rate of Ag.

Temperature

The temperature of the HNO_3 solution can be adjusted by the hotplate in order to have a reasonable dissolution rate of the metals. The dissolution rate decreases with time since the concentration of HNO_3 solution decreases with time. The process can be accelerated by increasing temperature. However, in order to reduce the energy consumption of the process, the highest temperature is controlled between 50-60 ℃.

Table 5.1

Metal contents in crystalline-Si solar modules by weight [47].

Metal in wafer-Si module	Content (weight %)
Al	10%
Si	~3%
Pb	<0.1%
Cu	0.6%
Ag	<0.006%

5.3 Sequential Electrowinning

After metal dissolution, the metals will be recovered by electrowinning. These metals can be recovered sequentially from the solution according to their reduction potentials, which is called sequential electrowinning. Since the solution contains multiple metals which have different reduction potentials, the applied voltage needs to be controlled precisely in order to recover these metals one by one.

The electrochemical system for sequential electrowinning is the three-electrode system which is shown in Fig. 5.3. Three electrodes contain a working electrode (W.E.), counter electrode (C.E.) and reference electrode (R.E.). The voltage is applied between the working electrode and reference electrode to introduce an electron current to the working electrode to recover metals. The system will apply an opposite voltage to the counter electrode to extract the same electron current in order to balance the electron current on working electrode. Very small current flows to the reference electrode due to the high resistance in the voltmeter. Since almost no current flows to the reference electrode, the potential on it

is fixed. As a result, the voltage applied between the working and reference electrode is precise, which can be used for sequential electrowinning.

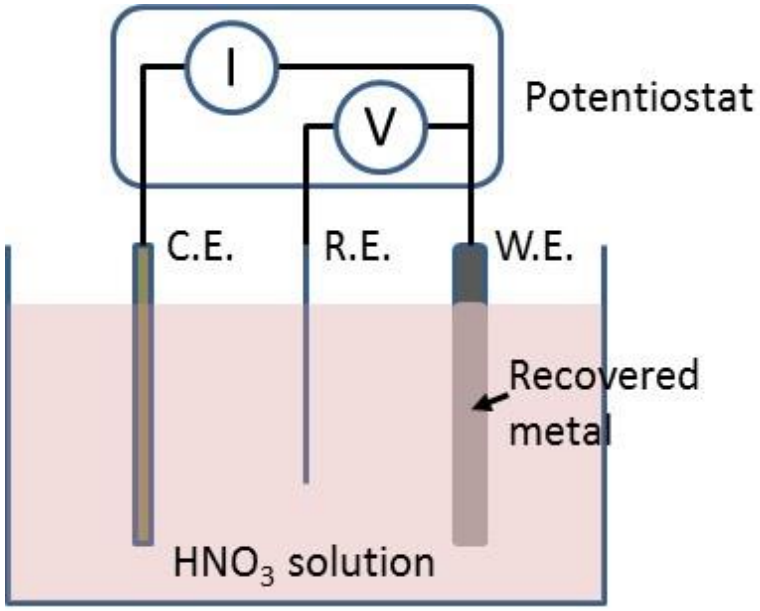

Fig. 5.3 Schematic of the three-electrode system for sequential electrowinning of multiple metals.

With the reference electrode, the voltage can be precisely controlled. The reduction potentials for metal ions can be identified by linear sweep voltammetry. By that, the voltage can be scanned versus the reference electrode linearly as Fig. 5.4(a). When the voltage is scanned to V_1, in Fig. 5.4(b) it starts to show a current at V_1, which means an electrochemical reaction occurs for certain metal ions due to electron transfer. Since the negative current refers to the cathodic current, the V_1 will be roughly assigned as the reduction potential of the metal ions which is the minimum energy to facilitate the reduction reaction of the metal ions. When the voltage is scanned to V_2, the current reaches the maximum, which gives highest reduction reaction rate. However, when the voltage is scanned to the voltage larger than V_2, the current starts to decrease because the metal ions

near the electrode are depleted too fast to supply for the reduction reaction. In the leached solution from c-Si solar modules, Ag^{+}, Cu^{2+} and Pb^{2+} have different reduction potentials. With the linear sweep voltammetry, their reduction potentials can be identified, respectively.

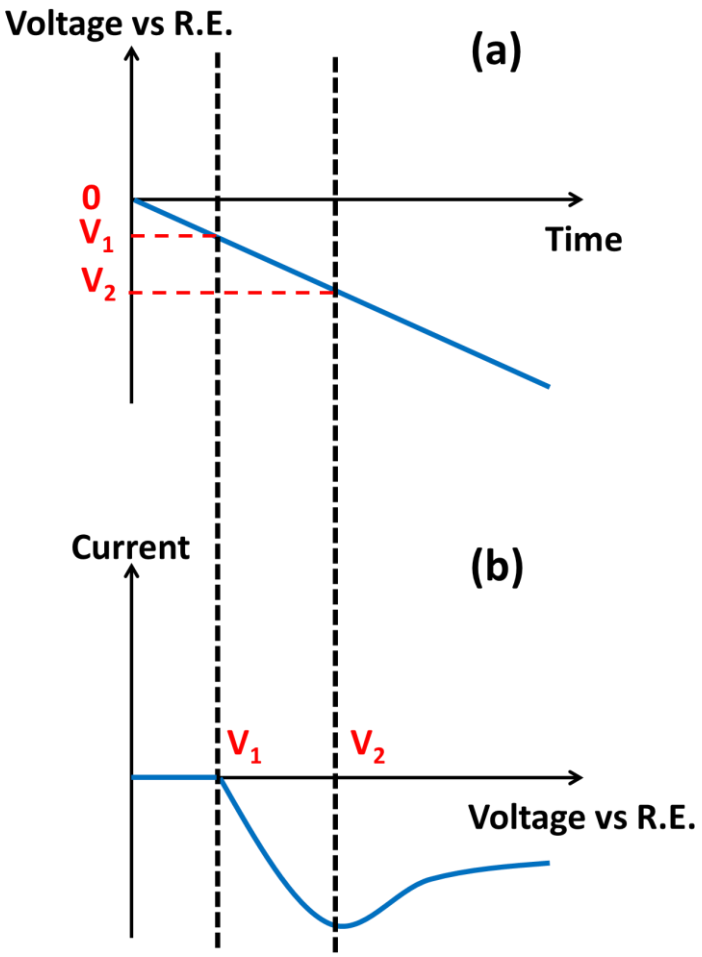

Fig. 5.4 Voltage versus time for linear sweep voltammetry (a) Current versus voltage for linear sweep voltammetry (b).

5.4 Experimental

To measure the metal recovery rate in electrowinning, a simulated leaching solution is utilized for the experiment. Metal contents in typical c-Si modules are listed in Table 5.1

[47]. As Table 5.1 does not specify the Sn content in Si modules, it is assumed that the Sn content is the same as Pb. Al does not dissolve in HNO_3 and its reduction potential is too negative to allow recovery by electrowinning from an aqueous solution. As a result, Al is not included in this study. 0.0431 g of Ag, 0.72 g of Sn, 0.72 g of Pb and 4.31 g of Cu pellets are added to a 100-ml beaker. Their weight ratios follow Table 5.1. The concentration of the HNO_3 solution is diluted to 11.4% to lower the risk of the process. An aqueous solution of 11.4% HNO_3 is poured into the beaker to dissolve the Ag, Pb, Sn and Cu pellets. The amount of HNO_3 solution is controlled to react with all the metals in the beaker and the pH of the final solution is between 0 and 1. If the pH is less than 0, it is found that Ag does not deposit on the Ti working electrode in electrowinning. The beaker is heated on a hotplate to 60˚C. After the metal pellets are completely dissolved, the solution is cooled down to 25˚C. The leaching solution after metal dissolution is shown in Fig. 5.5. The blue color is due to Cu^{2+} ions in the solution. The white precipitate at the bottom is SnO_2, as observed in previous studies [45,46]. The precipitated SnO_2 is recovered by filtration, but can be recovered by sedimentation as well.

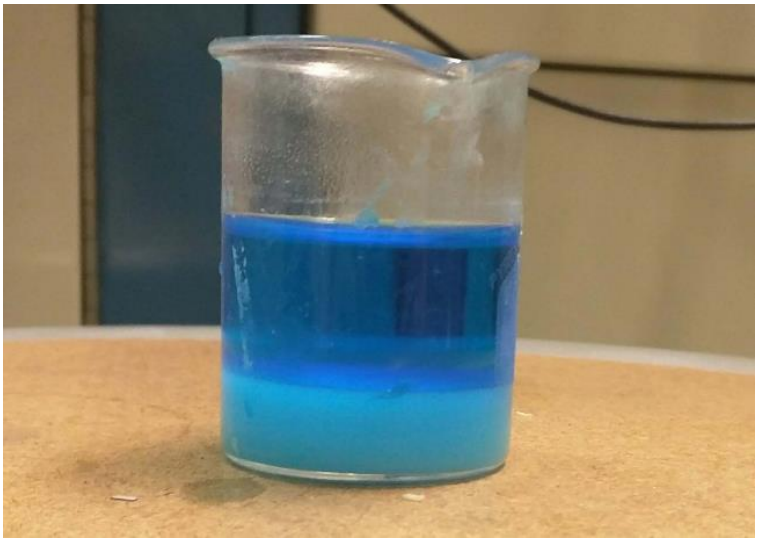

Fig. 5.5 The HNO_3 leaching solution after dissolution of four metals, Ag, Pb, Sn and Cu.

The leaching solution undergoes sequential electrowinning to recover the remaining metals, Ag, Cu and Pb. Fig. 5.3 illustrates the setup for sequential electrowinning, which involves three electrodes, a working electrode (W.E.), a counter electrode (C.E.) and a reference electrode (R.E.). Pt and Ti foils are used as the counter electrode and working electrode, respectively, since they are stable in concentrated HNO_3. An Ag/AgCl electrode is used as the reference electrode. A Gamry Reference 3000 potentiostat is used for electrowinning. Linear sweep voltammetry is performed on the leaching solution to measure the reduction potential for each of the three remaining metals, Ag, Pb and Cu. The scan rate is 10 mV/s. A progressively more negative voltage is then applied to the Ti working electrode to recover the metals one at a time. Each voltage is applied for 7000s. The deposit on the working electrode for each voltage is characterized by energy-dispersive x-ray spectroscopy (EDX). For maximum recovery rates, Ag recovery and Cu recovery with applying specific voltage characterized above are performed from another new

leached solution until the reaction current approaches zero. The solution is stirred to speed up the diffusion of Ag^{+} and Cu^{2+} ions.

5.5 Results and Discussions

Fig. 5.6(a) is the linear sweep voltammetry of the leaching solution. There is a large cathodic current at ~0.1 V vs. the Ag/AgCl reference electrode, indicating that something is reduced. If Fig. 5.6(a) is zoomed in between 0.45 V and 0 V as shown in Fig. 5.6(b), it shows two reduction reactions. The first reduction reaction begins at ~0.43 V and reaches a peak at ~0.35 V. The second reduction reaction occurs at ~0.1 V. Since Ag is the noblest metal and Cu is the second noblest in the solution, the first and second reduction reactions are attributed to Ag and Cu reduction, respectively. The window to separate Ag from Cu is between 0.43 V and 0.25 V from Fig. 5.6(b).

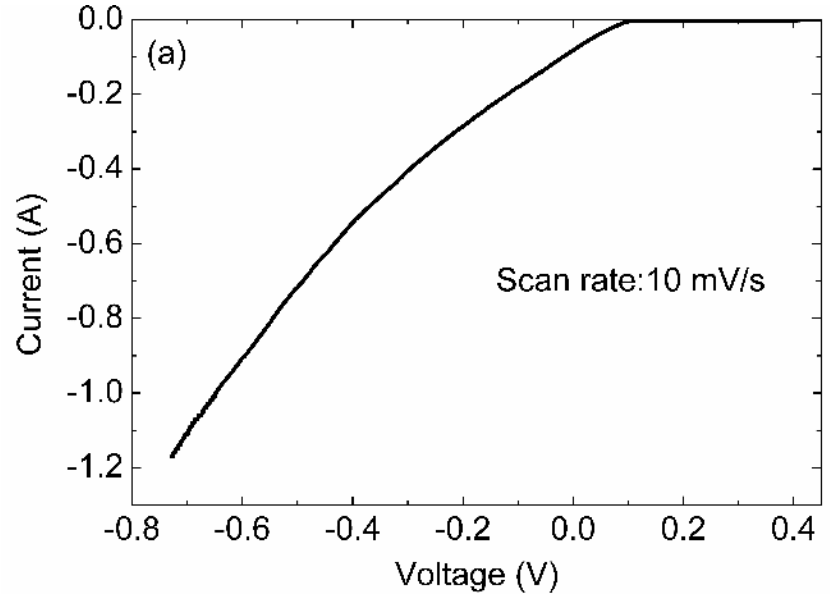

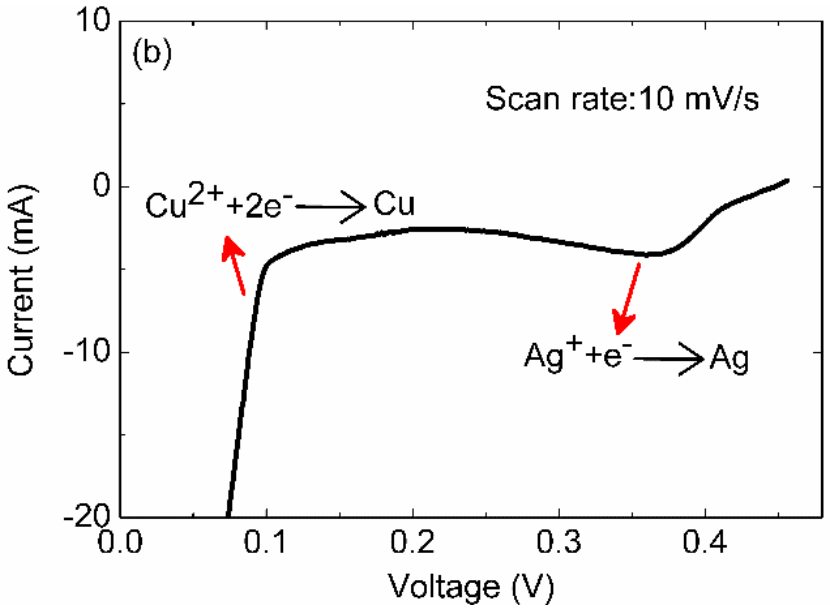

Fig. 5.6 Voltammetry of the leaching solution (a) and zoom-in of (a) between 0.5 V and 0 V vs. Ag/AgCl (b).

The concentrations of Ag^{+}, Cu^{2+} and Pb^{2+} in the simulated leaching solution are 5×10^{-3} M, 0.85 M and 0.04 M, respectively. Their reduction potentials from the Nernst equation are 0.45 V, 0.128 V and –0.38 V vs Ag/AgCl. The theoretical reduction potentials for Ag and Cu are very close to those from the voltammetry. Since the concentration of Cu^{2+} is much higher than Pb^{2+}, its large reduction current shadows the reduction reaction of Pb^{2+} in the voltammetry.

Fig. 5.7 shows EDX analysis of the deposits under different voltages on the Ti working electrode. Ti peaks show up due to the Ti electrode. Between 0.35 V and 0.25 V, the deposits contain only Ag. However, when the voltage is less than 0.2 V, Cu starts to show up in the EDX spectra. As a result, the window to recover 99% pure Ag is between 0.45 V and 0.25

V vs. Ag/AgCl since the detection limit of EDX is typically about 1%. The concentration of Ag in the solution decreases with time. The Nernst equation states that, when the concentration decreases, the reduction potential becomes more negative. 0.3 V vs. Ag/AgCl is chosen for Ag recovery.

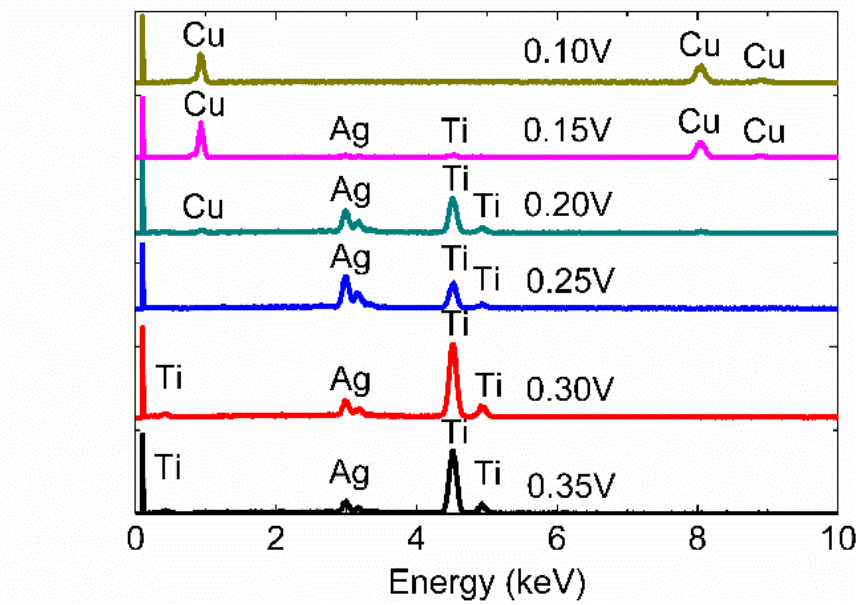

Fig. 5.7 EDX spectra of the deposits on the Ti working electrode under different voltages vs. Ag/AgCl.

Fig. 5.8 is the current vs. time plot for Ag recovery with the voltage on the Ti working electrode at 0.3 V vs. Ag/AgCl. The total electrowinning time is 20,000 s. The reduction current decreases with time as the concentration of Ag^+ decreases over time until it approaches zero. Fig. 5.9 is EDX analysis of the deposit at 0.3 V vs. Ag/AgCl for 20,000 s. It shows only Ag peaks from the recovered Ag and Ti peaks from the Ti electrode. The

purity of the recovered Ag is at least 99%. The recovery rate of Ag in this experiment is 74%. This is obtained by measuring the weight gain of the Ti electrode and comparing it with the amount of Ag in the solution. By minimizing kinetic factors, the recovery rate of Ag can be significantly improved. The current efficiency of Ag recovery is 99.7%.

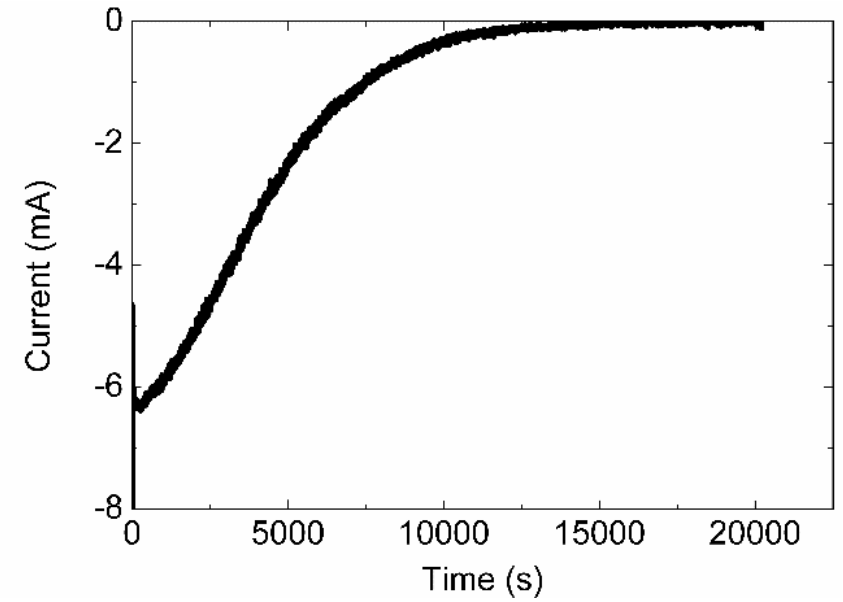

Fig. 5.8 Current-time plot for Ag recovery at 0.3 V on the Ti working electrode vs. Ag/AgCl.

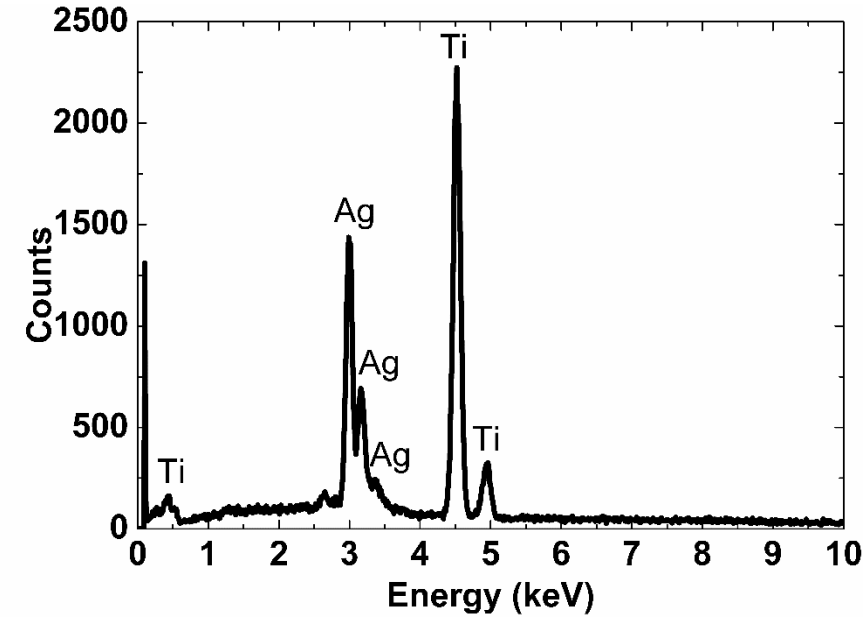

Fig. 5.9 EDX spectrum of the deposit on the Ti working electrode at 0.3 V vs. Ag/AgCl for 20,000 s.

Fig. 5.10 compares the voltammetry of the leaching solution before and after Ag recovery. After Ag recovery, the Ag^{+} reduction reaction at ~0.35 V disappears and only the reduction reaction of Cu^{2+} is still present. This further proves that only Ag is removed from the solution during Ag recovery.

Cu recovery is performed after Ag recovery. –0.3 V vs. Ag/AgCl is applied to the Ti electrode. The reduction reaction of Pb^{2+} is shadowed by the reduction reaction of Cu^{2+} in Figs. 5.6 and 5.10, and the theoretical reduction potential of Pb^{2+} from Eq. (1) is –0.38 V vs. Ag/AgCl. Fig. 5.11 shows EDX analysis of the deposit on the Ti electrode at –0.3 V for 24 hrs. There are Cu peaks but there is no Pb peak in EDX, indicating that Cu with 99% purity is recovered from the Pb^{2+}-containing solution. The Ti peaks are not present as the

Cu deposit is thick. The oxygen peak is due to oxidation of Cu on the Ti working electrode. The recovery rate of Cu is currently 83%.

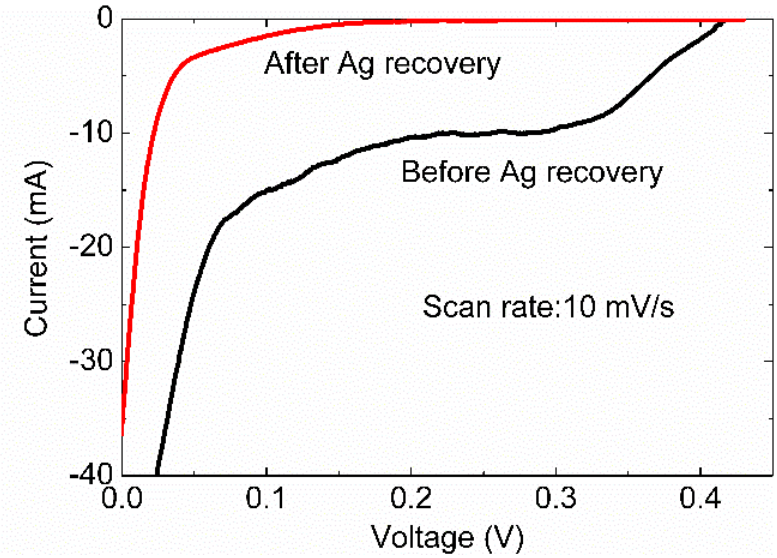

Fig. 5.10 Comparison of voltammetry of the leaching solution before and after Ag recovery.

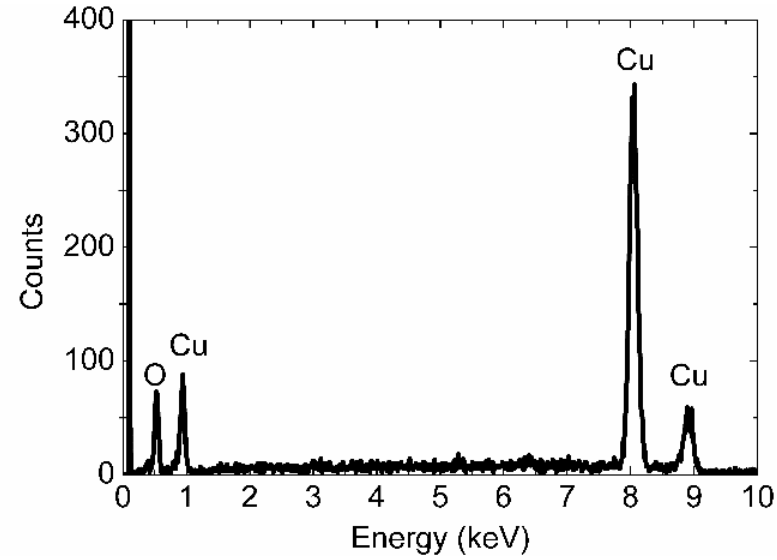

Fig.5.11 EDX spectrum of the deposit on the Ti working electrode at –0.3 V vs. Ag/AgCl for 24 hrs.

It is found that Pb^{2+} ions deposit on the Pt counter electrode as PbO_2 during Cu recovery, which is observed in a previous study [46]. The reaction of PbO_2 does not occur during Ag recovery. The reason for that is the concentration of Cu is much higher than that of Ag in the solution. During the recovery, the current of Cu recovery is much higher than that of Ag recovery on the working electrode. As a result, the potentiostat will drive a higher opposite voltage on the counter electrode in order to balance this higher current and then the higher opposite voltage drives the PbO_2 reaction on the counter electrode. Fig. 5.12 is EDX analysis of the Pt electrode after Cu recovery. Pb peaks are present, indicating that when Cu is recovered on the Ti working electrode, Pb is also recovered on the Pt counter electrode from the solution. The oxygen peak is small, maybe due to the nonstoichiometric PbO_x ($x<2$) on the Pt counter electrode. The solution after Cu recovery for 48 hrs is investigated by inductively coupled plasma optical emission spectroscopy (ICP-OES). The results are listed in Table 5.2. Ag and Cu are largely removed. The Sn concentration is high because the filtration of SnO_2 was done only with a simple filter paper. With the Pb concentration at 92 ppm and the volume of the solution at 60 ml, the amount of Pb in the solution is ~5.5 mg. This is only 0.76% of the Pb in the starting solution, i.e. over 99% of the Pb^{2+} ions are removed from the solution during Cu recovery and the solution is almost free of toxic Pb.

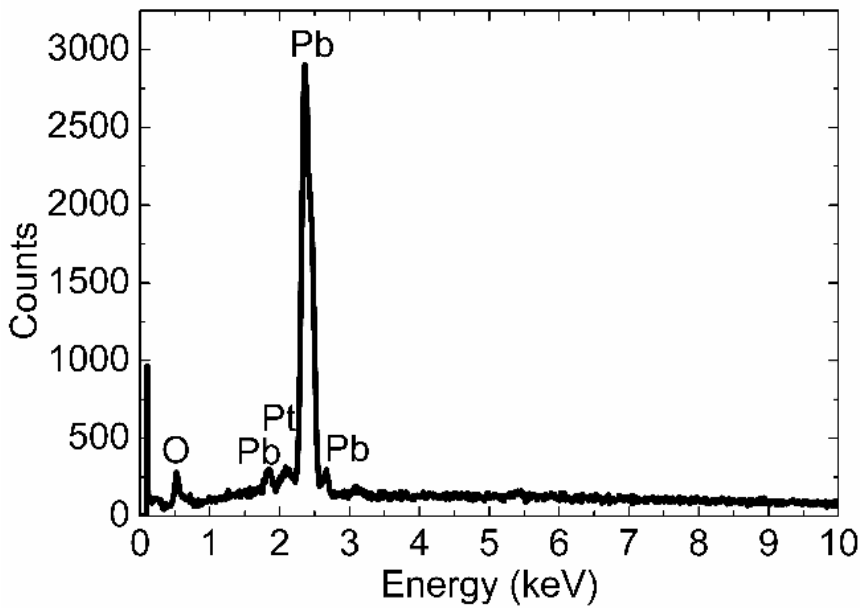

Fig. 5.12 EDX spectrum of the deposit on the Pt counter electrode after Cu recovery for 24 hrs.

Table 5.2

Metal contents in leaching solution after Cu recovery for 48 hours.

Metal	Content (ppm)
Ag	0.034
Cu	3.38
Pb	92.1
Sn	426

74% Ag and 83% Cu are recovered. However, there are several reasons to restrict the recovery rate for the sequential electrowinning.

Limitation of Thermodynamics

From Nernst equation, the reduction potential of Ag will become more negative as the concentration of Ag ion in the solution becomes less. When the reduction potential of Ag decreases to the reduction potential of Cu, which means their reduction potentials overlap, Ag and Cu will be recovered together and the pure Ag can not be recovered. As a result, there is a certain amount of Ag which can not be recovered individually due to the overlap of the reduction potentials, which is the limitation of thermodynamics.

Amount of HNO_3 in the solution

The amount of HNO_3 needs to be controlled to dissolve the metals from c-Si solar modules. If the amount of HNO_3 applied is too large, the huge amount of residual HNO_3 in the solution will redissolve the recovered metal during the electrowinning and then lower the recovery rate. The efficient way to control the amount of HNO_3 applied is that monitoring pH value change during the metal dissolution.

Filtration

SnO_2 is filtrated during the process. During the process there is some residual solution remaining on the filter paper. The mass loss can be improved if the vacuum system can be introduced to assist the process of the SnO_2 filtration to reduce the residual solution on the filter paper.

Dendritic Deposition

The morphology of electrodeposition is affected by the current density. The electrode for the working electrode is the Ti foil. On the surface of the Ti foil, the recovered metals represent the morphology of thin films. However, at the edge of Ti foil, the deposition of dendrites is formed by the recovered metals. The dendrites are brittle and very easy to drop

from the Ti foil. Some of the dendritic metals dropped to the bottom of the beaker during electrowinning and some of them are lost during the rinse after electrowinning.

The issue can be improved if a larger size of Ti foil is used. A larger Ti foil has a larger surface to edge area ratio, which can reduce the proportion of the edge effect of the Ti foil. Another solution is to use metallic beaker as the working electrode, which can preserve all the recovered metal in the beaker to reduce the loss.

5.6 Metal Recycle for Crystalline-Si Solar Modules on a Large Scale

Fig. 5.13 shows scaling up for the process of the metal recycling. The HNO_3 with a certain concentration in the large tank is prepared and then c-Si solar modules are put into the solution for metal dissolution. A pH meter is used to measure the pH value of the solution to monitor the concentration of HNO_3 in the solution. When the pH of the solution increases to a certain value, which means all the HNO_3 in the solution is almost consumed, then the solution can be used for electrowinning due to higher recovery rate with less HNO_3 in the solution.

The material of the counter electrode is an issue for the mass production, which suffers from the oxidation potential and the low pH solution. Pt shows its stability under the oxidation potential plus the low pH environment. However, Pt is too expensive for scaling up. The replacement of the materials for the counter electrode needs to be found.

When Ti is used as the counter electrode, Ti electrode will react with the solution and then be etched during the Cu recovery. As a result, Ti is not suitable as the counter electrode for the process.

W and Mo look stable under the condition. However, the three-electrode system can not sustain the desired voltage due to overload when W and Mo are used as the counter electrode, which means the counter electrode can not supply enough current to balance the current on the working electrode so the voltage between working and reference electrode can not be fixed. The reason is that W and Mo under low pH and oxidation potential will form the oxide on their surface as the passivated film from their Pourbaix diagrams. The counter electrode becomes an insulator and can not conduct the current. The entire system suffers from the overload and can not control the voltage. As a result, W and Mo are not suitable as the counter electrode. A possible solution is Ti electrode with Pt coating, which can lower the cost of the counter electrode and also sustain the chemical and electrical stability during the electrowinning.

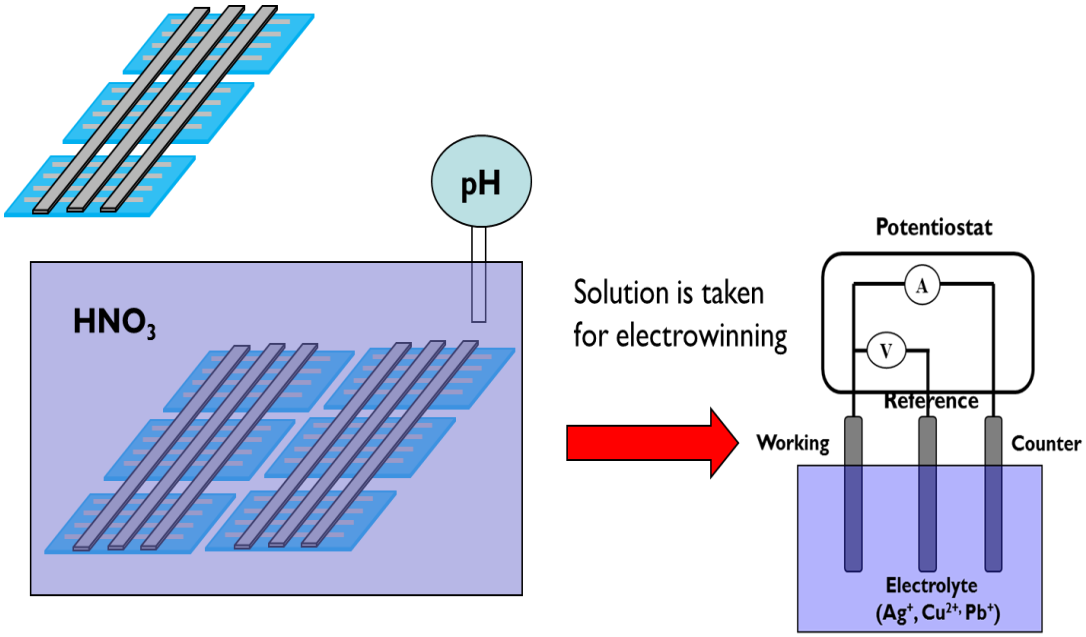

Fig. 5.13 Scaling up for metal recycling from c-Si solar modules.

5.7 Summary

The metal recycling process from c-Si solar modules is developed. The nitric acid solution with 11.4% concentration is used for Ag, Cu, Sn, Pb leaching. Ag, Cu, Pb are dissolved into solution and Sn reacts with HNO_3 to form SnO_2 which can be filtered. The amount of HNO_3 solution is controlled to completely leach and react all of Ag, Cu, Sn and Pb and also have pH >0 of the solution after leaching. Then the solution with Ag^+, Cu^{2+} and Pb^{2+} is sent for the electrowinning. Three-electrode system is used for applying the accurate voltage to recover these metals one by one. Ag and Cu at least 99% purity can be recovered on the working electrode with 74% and 83% recovery rate, respectively. Pb will be recovered as PbO_2 on the counter electrode during Cu recovery. Larger than 99% amount of Pb is gone from the solution after Cu recovery. The final solution is almost Pb free.

CHAPTER 6

RECYCLE SOLAR GRADE Si FROM C-Si SOLAR CELLS

6.1 Introduction

The cells after metal dissolution have the structure in Fig. 3.2(b). They are immersed into an aqueous solution of 10% HF for 15 min to remove the SiN_x layer, Al-Si alloy and Al back electrode. The structure of the remaining cells is shown in Fig. 3.2(c) which is the Si part of c-Si solar cells. The purpose of solar-grade Si recovery is to etch off the front emitter (n^+ Si) and back-surface field Si (p^+Si) and to recover the base (p Si).

Heavily doped n^+ Si emitter

On the fronside, the n^+ heavily doped Si which is emitter is formed by P diffusion. Fig. 6.1 is the P diffusion process by $POCl_3$. Liquid state $POCl_3$ is the common source of P. Carrier gas nitrogen (N_2) and reaction gas oxygen (O_2) flow through liquid $POCl_3$ and bring it into the tube furnace. $POCl_3$ reacts with O_2 forming solid P_2O_5 on the Si wafer surface, and then P_2O_5 further reacts with Si to generate P. With the high temperature, P diffuses into Si surface and forms n^+ emitter. The reactions are:

$$\boldsymbol{POCl_3 + O_2 \rightarrow P_2O_5 + Cl_2} \quad (6.1)$$

$$\boldsymbol{P_2O_5 + Si \rightarrow SiO_2 + P} \quad (6.2)$$

A layer of PSG is formed on the Si and then removed by HF. The highest temperature for the process is about 900℃ in order to drive P into Si to form n^+ Si emitter. Typically, the thickness of the emitter is about 0.7 to1 μm. The purpose of n^+ Si emitter is to form the p-n junction with p-type Si base for driving minority carriers to provide the power.

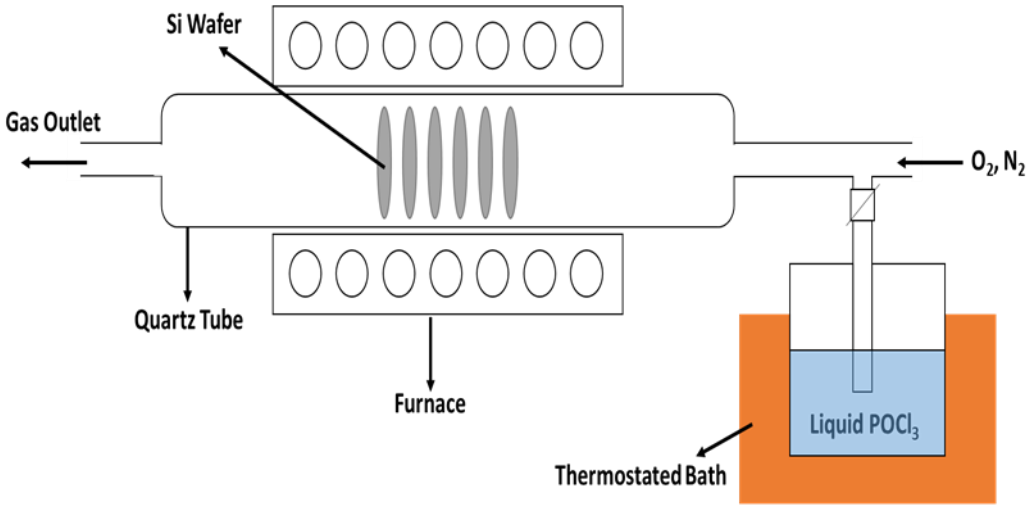

Fig. 6.1 Schematic of $POCl_3$ diffusion by diffusion furnace [48].

Heavily doped p^+ Si back surface field

On the backside, p^+ Si back surface field (BSF) is formed by the interaction between Si and Al paste printed on the Si by screen printing at high temperature. The purpose of BSF is to passivate the rear surface to minimize the impact of rear surface recombination velocity. With BSF p^+ Si adding on the rear side of the p-Si base, the minority carriers in p Si which are electrons have less chance to be trapped by the rear surface due to the potential difference between p^+ and p Si. As a result, the surface recombination decreases, and the efficiency of the solar cell increases by BSF [49–51].

The Al paste first is printed on c-Si solar cells on the backside by screen printing. For most of the c-Si solar cells, they have full area Al printing. After full area Al printing, the cells are sent to the belt furnace for high-temperature firing. The firing temperature is typically around 800℃ which is higher than the melting point of Al (660℃) to accelerate the Al-Si alloying to form BSF. Figs. 6.2 (a) to (e) are the BSF forming process on the

backside of c-Si solar cells step by step [52,53]. The Al paste is printed on the Si cell as Figs. 6.2(a) to (b). Then Fig. 6.2 (c) shows the cell is put into high-temperature belt furnace for firing. The Al paste starts to melt. Then the Si in the p-Si base diffuses into the melting Al paste to form the Al-Si melt. Fig. 6.2(d) is the cells during the cooling stage. The Al-Si melt begins to solidify. Si atoms in the melt diffuse to the bottom of the melt to form the Al p^+ Si BSF since the p-type Si base provides the nucleation sites with lower activation energy for the nucleation. As the Si atoms in the melt diffuse to form the p^+ Si BSF, the concentration of Si in the melts decreases. Fig. 6.2(e) is the cell cooled down to room temperature. The Al-Si melt becomes Al-Si alloy. The doping concentration of the Al p^+ BSF in commercial c-Si solar cells is about 10^{19} cm^{-3}. Typically, the thickness of the Al p^+ BSF is about 7-10 μm.

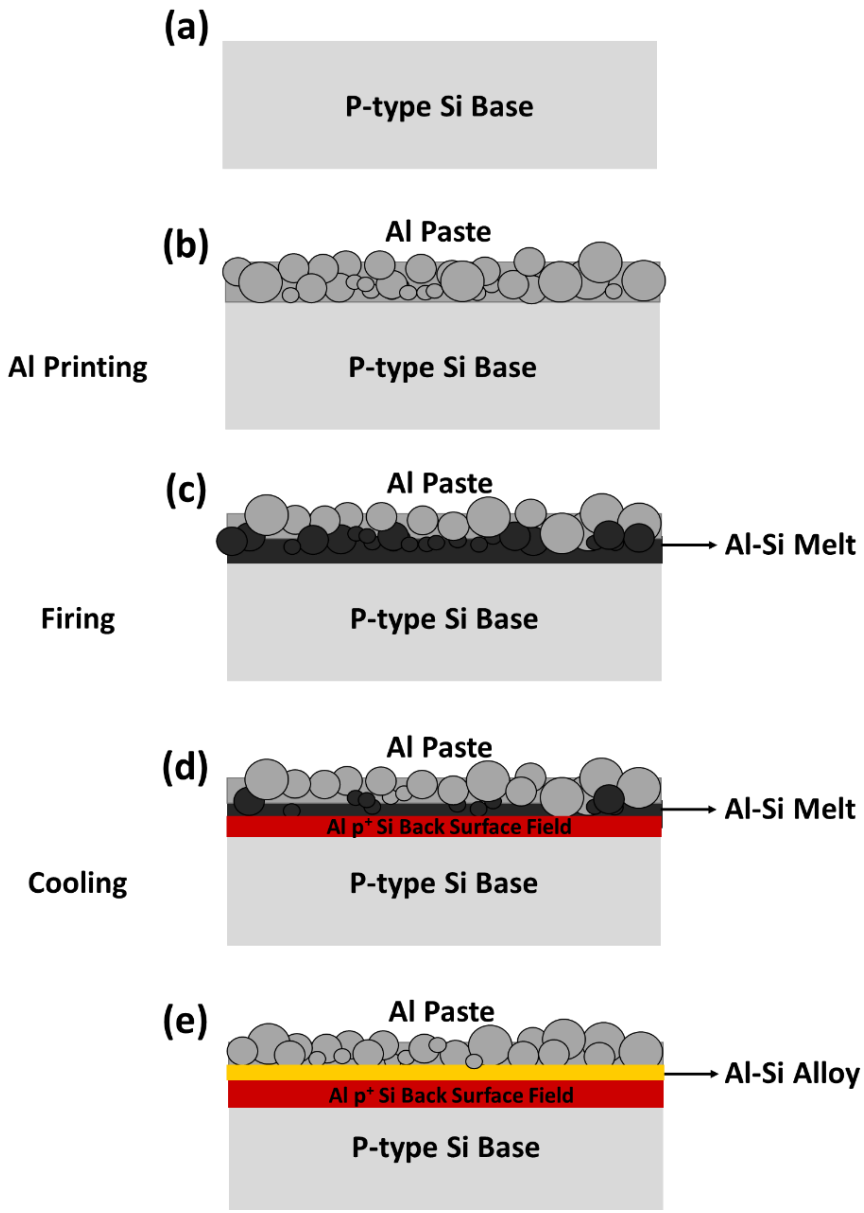

Fig. 6.2 Schematic for the screen printing and firing for c-Si solar cells: before Al printing (a); after Al printing (b); firing (c); cooling (d); finish (e)

Two studies for solar grade Si recovery [26]. The first study is to optimize the conditions of NaOH etch for the highest etch rate of Si. The reason why NaOH is used for Si etch is the reasonable etch rate and safety. The etch rate of NaOH for Si is less than 1 μm/min. Another Si etch solution such as HNO_3/HF solution has higher etch rate but is more dangerous [54–57]. Since the heavily doped Si in c-Si solar cells is around 10 μm, the etch rate of Si can not be too fast in order to control the etch time precisely to just remove the heavily doped Si in c-Si solar cells to recover the maximum amount of the solar grade Si for recycling. Furthermore, HNO_3 is used for metal recycling, which will generate the acidic waste. In the solar grade Si recycling, NaOH is chosen as the etch solution which can neutralize the acidic waste to lower the risk of the final waste.

The second study is to maximize the amount of solar-grade Si recovered. There are many ways to monitor the etch process such as secondary ion mass spectrometer (SIMS), electrochemical capacitance profiler (ECV) or glow discharge mass spectrometry (GDMS) which can show the doping profile of Si. The techniques listed above are destructive, time-consuming. However, the technique to monitor the etch process needs to be time-efficient. Fig. 6.3 is the flowchart for recycling solar grade Si. There are a lot of solar cells from different companies and their heavily doped Si thicknesses are different. In the case, the throughput will be affected seriously if the technique to monitor the etch process is too complicated and time-consuming. As a result, the technique to monitor the process must be easy and quick.

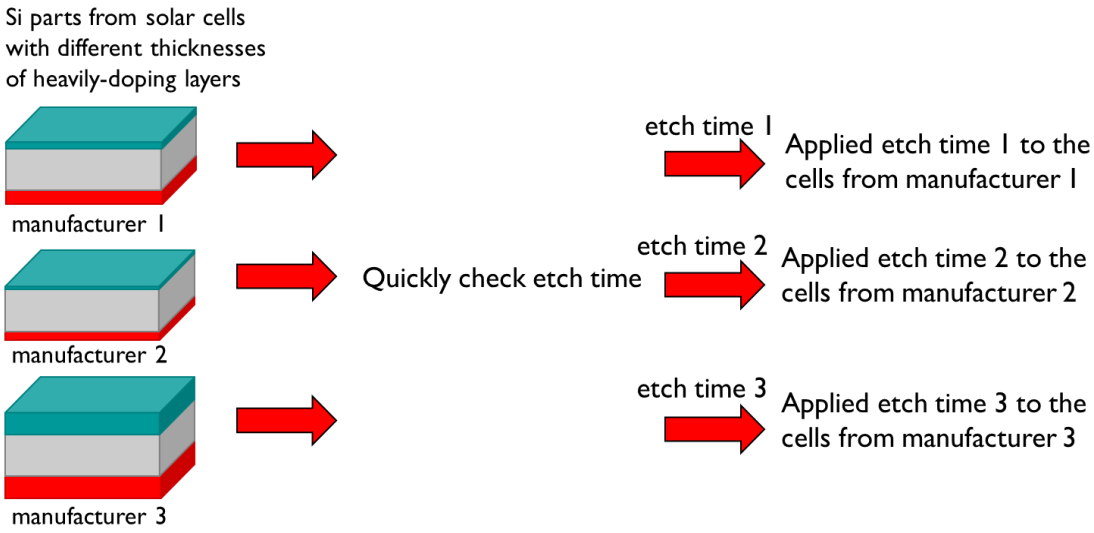

Fig. 6.3 Process flow for solar grade Si recycle from c-Si solar cells

6.2 Experimental

To optimize the NaOH etch conditions, Si wafers are immersed into aqueous NaOH solutions of various concentrations from 1% to 50% at 25˚C, as the saturated NaOH concentration in water is ~50% at 25˚C. The weight of the Si wafers is measured every 15 min and then converted to wafer thickness by the following equation:

$$Thickness = \frac{Weight}{Area \times Density} \qquad (6.3)$$

It is assumed that the area of the Si wafer does not change after etch. Once the NaOH concentration for the highest etch rate is determined, the temperature of the NaOH solution is raised to 50˚C to further increase the etch rate.

To remove the emitter and back-surface field, commercial monocrystalline-Si (mono-Si) solar cells are used. They go through HNO_3 and HF to remove the front electrode, back electrode and SiN_x layer. The remaining cells have the structure in Fig. 3.2(c). They are

etched in an aqueous NaOH solution under the conditions identified above. Every 15 min, the cells are lifted from the NaOH solution and their sheet resistances are measured by a 4-point probe on both the front and back sides. The reciprocal sheet resistances are then plotted against etch time to determine the precise moment when the heavily-doped emitter and back-surface field are just removed.

6.3 Results and Discussion

Fig. 6.4(a) shows the thickness loss of Si wafers as a function of etch time at 25˚C under different NaOH concentrations from 10% to 50%. Etch of Si starts after 15 min with stable slopes, i.e. constant etch rates, for all concentrations. The slow etch during the first 15 min suggests the presence of native oxide which hinders the etch rate. This assumption is verified in Fig. 6.4(b), which shows the thickness loss of two Si wafers in 10% NaOH, one with and the other without 10% HF pretreatment for 15 min. With HF pretreatment, the wafer shows a stable slope from the beginning, while the other wafer initially has little etch and then a stable slope after 15 min. The etch rate of native oxide by NaOH is lower than that of Si. With native oxide, there are two stages in the etch: (1) an oxide etch stage (first 15 min) and (2) a Si etch stage (dashed circle). It is noted that the etch rate, i.e. the slope, for the HF-treated wafer is the same as the wafer without HF pretreatment after 15 min. This is clearly the Si etch stage.

From Fig. 6.4(a), the etch rate in the Si etch stage increases when the NaOH concentration decreases. In order to increase the etch rate, the NaOH concentration is reduced below 10%.

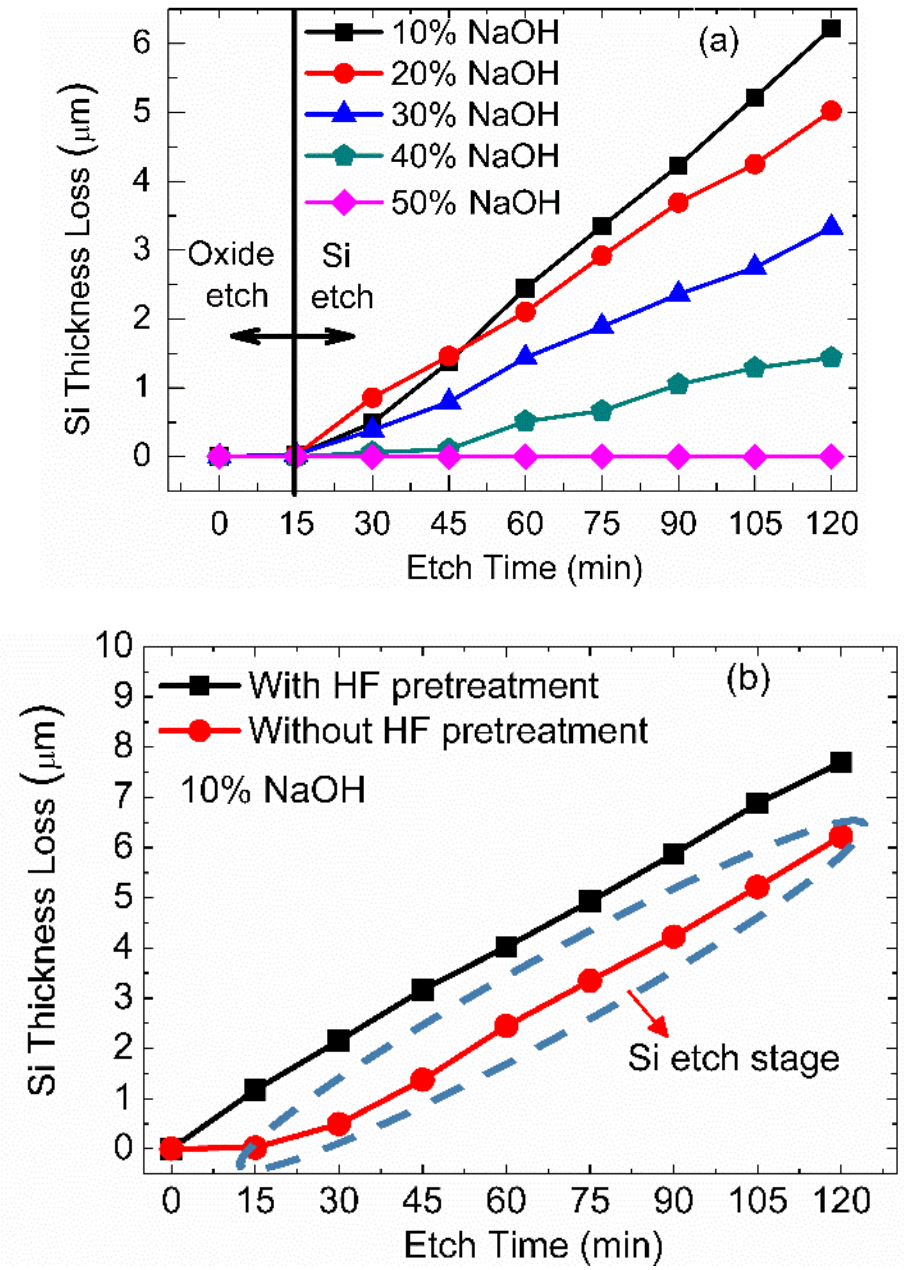

Fig. 6.4 Thickness loss of Si in NaOH solutions of various concentrations at 25˚C (a) and with or without HF pretreatment (b).

Fig. 6.5 is the thickness loss of Si wafers as a function of etch time in 1%, 3%, 5% and 10% NaOH aqueous solutions at 25˚C. None of these wafers goes through HF pretreatment, so they all have the oxide etch stage. The time for oxide etch is 15 min, 30 min, 45 min and 60 min for 10%, 5%, 3% and 1% NaOH, respectively. After oxide etch, all the wafers show stable slopes indicative of Si etch. From the slopes the etch rate of Si is determined, as shown in Fig. 6.6 The 3% NaOH solution shows the highest Si etch rate, which is 0.082 μm/min.

The etch reaction of Si by NaOH as follow:

$$Si_{(s)} + 2NaOH_{(aq)} + H_2O_{(aq)} \rightarrow Na_2SiO_{3(aq)} + H_{2(g)} \quad (6.4)$$

From the reaction, NaOH and H_2O must exist simultaneously to etch Si. As result, the etch rate is determined by the concentration of NaOH and H_2O. The maximum etch rate is also compromised between the concentrations of NaOH and H_2O and is reached at 3% NaOH solution. However, the native oxide etch reaction is

$$SiO_{2(s)} + 2NaOH_{(aq)} \rightarrow Na_2SiO_{3(aq)} + H_2O_{(aq)} \quad (6.5)$$

Native oxide only needs NaOH for etching. The etch rate is determined only by NaOH. As a result, when the concentration of NaOH increases, the etch rate of the native oxide increases and the time for native oxide etch decreases.

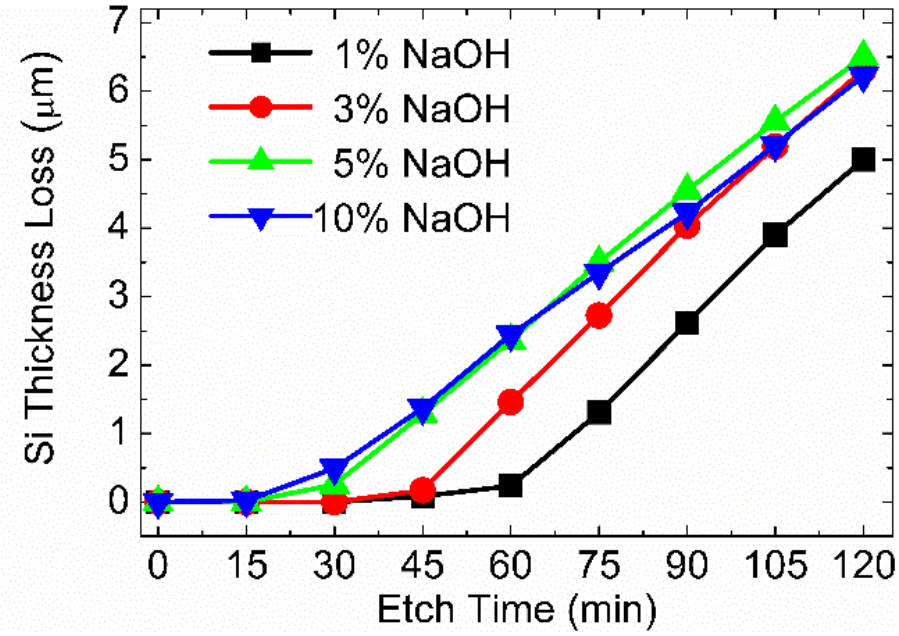

Fig. 6.5 Thickness loss of Si in 1%, 3%, 5% and 10% NaOH aqueous solutions at 25˚C.

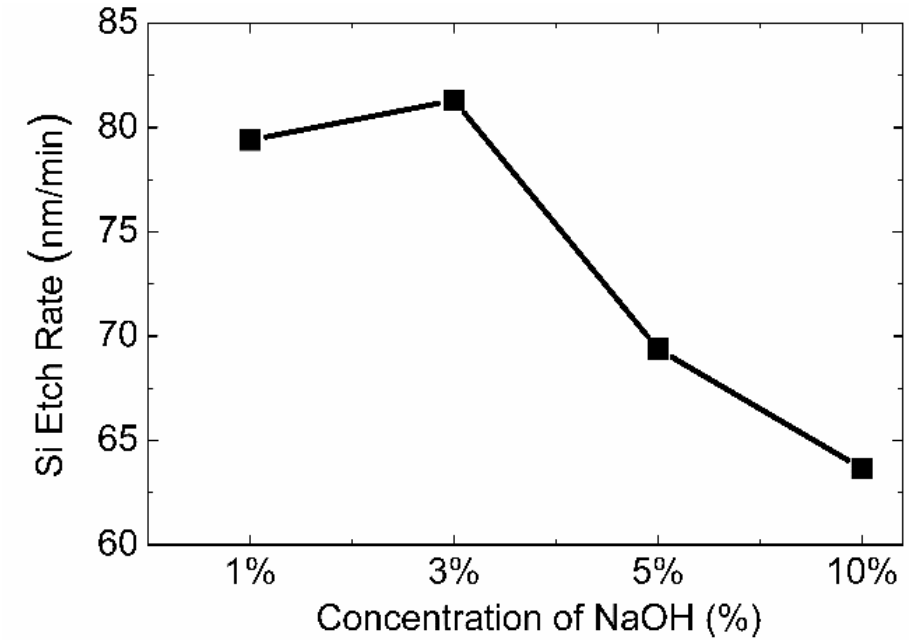

Fig. 6.6 Si etch rate in 1%, 3%, 5% and 10% NaOH aqueous solutions at 25˚C.

The back-surface field is ~10 μm thick. Even at 0.082 μm/min, the etch rate is still too low for the back-surface field. In order to increase the etch rates of native oxide and Si, the 3% NaOH solution is heated to 50˚C. This temperature can be achieved by exposing the NaOH solution under sunlight. Fig. 6.7 shows the thickness loss of a Si wafer as a function of etch time in a 3% NaOH aqueous solution at 50˚C. There is no oxide etch stage at 50˚C and the Si etch rate is around 0.53 μm/min. At this etch rate, the back-surface field can be removed in ~20 min. 3% NaOH at 50˚C are the conditions used for actual cell etch.

Commercial mono-Si cells with the structure in Fig. 3.2(c) are immersed into a 3% NaOH aqueous solution at 50˚C. Every 15 min, the cells are lifted out of the NaOH solution and their sheet resistances are measured from both the front and back sides by a four-point probe. Fig. 6.8 plots the reciprocal sheet resistance of a cell as a function of etch time. Initially, the sheet resistances from the two sides are different because the sheet resistance from the front side is that of the n^+ emitter, and the sheet resistance from the backside is that of the p^+ back-surface field in parallel with the p-type base. After 15 min, the two sheet resistances become identical. This happens when the n^+ emitter is completely removed. As a result, no matter which side the sheet resistance is measured from, it is always the sheet resistance of the p^+ back-surface field in parallel with the p-type base. After 30 min, the plot changes its slope. This indicates the complete removal of the p^+ back-surface field and only the lightly-doped p-type base is left. As soon as the slope changes, the etch should be stopped to recover the maximum possible amount of solar-grade Si from the cell.

The backside of the cell contains a p layer and a p^+ layer in parallel. The reciprocal sheet resistance of the backside is:

$$\frac{1}{R_S} = \frac{\rho_{p+} w_p + \rho_p w_{p+}}{\rho_{p+} \rho_p} \tag{6.6}$$

where R_S is the measured sheet resistance, ρ_{p+} the resistivity of the p^+ layer, ρ_p the resistivity of the p layer, w_{p+} the thickness of the p^+ layer and w_p the thickness of the p layer. Eq. (6.6) indicates that the measured sheet resistance of the backside is a function of the thicknesses of the p and p^+ layers. In Fig. 6.7, the thickness of the Si wafer has a linear relation with etch time in 3% NaOH at 50˚C. As a result, the reciprocal sheet resistance of the backside is a linear function of etch time. This is verified by the straight line for the backside between 0 min and 30 min in Fig. 6.8.

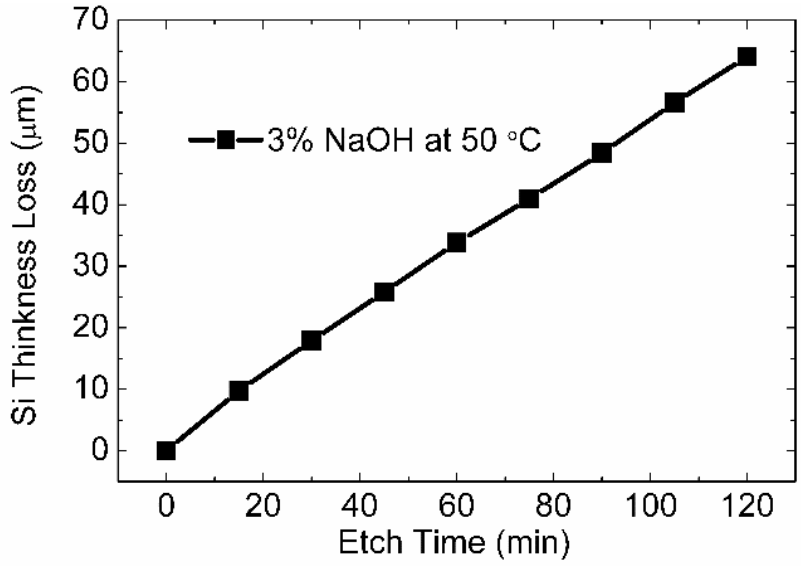

Fig. 6.7 Thickness loss of Si in a 3% NaOH aqueous solution at 50˚C.

When the p^+ layer is completely removed, the reciprocal sheet resistance of the backside becomes:

$$\frac{1}{R_S} = \frac{w_p}{\rho_p} \tag{6.7}$$

At this stage, the reciprocal sheet resistance is also linear with etch time because the thickness of the p layer has a linear relation with etch time. However the reciprocal sheet resistance shows a different slope. This is why the slope changes at 30 min in Fig. 6.8, and the point of slope change indicates that the p^+ back-surface field has just been completely removed. Since w_p decreases with etch time at a constant rate, Eq. (6.7) can be rewritten as:

$$\frac{1}{R_S} = -\frac{r \times t}{\rho_p} + C \tag{6.8}$$

where r is the Si etch rate, t the etch time and C a constant related to the initial thickness of the p-type base. With Eq. (6.8), one can find the resistivity of the p-type base, ρ_p, by dividing the Si etch rate with the absolute value of the slope between 30 min and 120 min in Fig. 6.8. The etch rate of Si is 0.53 μm/min and the fitted slope is -3.77×10^{-5} □/ Ω-min. The ρ_p calculated is thus 1.41 Ω-cm, which is in agreement with the specifications of the solar grade Si.

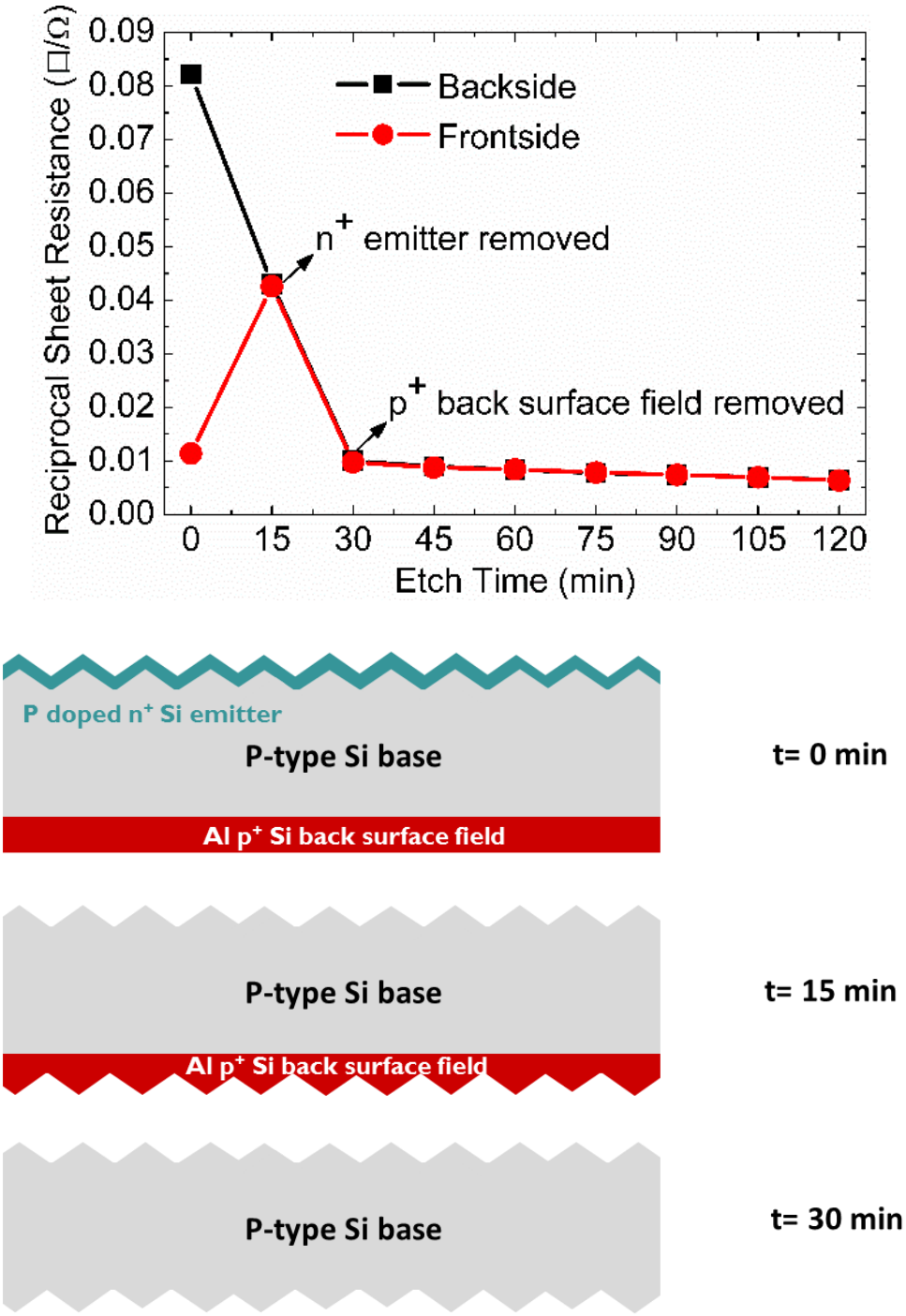

Fig. 6.8 Reciprocal sheet resistance of a Si cell in a 3% NaOH solution at 50˚C as a function of etch time.

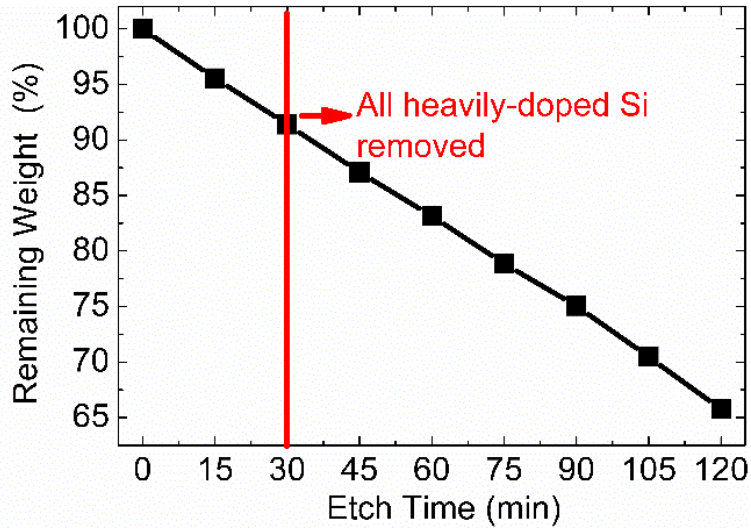

Figure 6.9 Remaining weight of a Si cell in a 3% NaOH solution at 50˚C as a function of etch time.

The remaining weight of a Si cell as a function of etch time has also been measured, as shown in Fig. 6.9. A 30-min etch removes all the heavily-doped layers. Fig. 6.9 reveals that after 30 min, the remaining weight is ~91% of the starting Si, i.e. the amount of solar-grade Si recovered by sheet resistance monitoring is over 90%.

6.4 Scanning Electron Microscope for Proving BSF p^+ Si Removal

Scanning electron microscope (SEM) can show the contrast on semiconductors between different doping concentrations, which could be used to show the contrast between back surface field p^+ Si and p-type Si base. By the observation of the contrast, the etch time to remove back surface field p^+ Si can be controlled.

The mechanism of contrast between p^+ Si and p Si by SEM can be explained by the energy band diagram. Fig. 6.10 is the energy band diagram of p^+ Si and p Si. From the working principle of SEM, the electron beam is emitted from the electron gun to the

material and the secondary electrons are knocked out from the materials. The secondary electrons are collected by the detector of SEM to form the image. From Fig. 6.10, the energy requirement of the secondary electrons from the valence band of p^+ Si to the detector is less than that of secondary electrons from the valence band of p Si to the detector. As a result, more secondary electrons from p^+ Si can reach the detector than those from p Si. The p^+ Si in the image of SEM will show brighter than p Si to form the contrast.

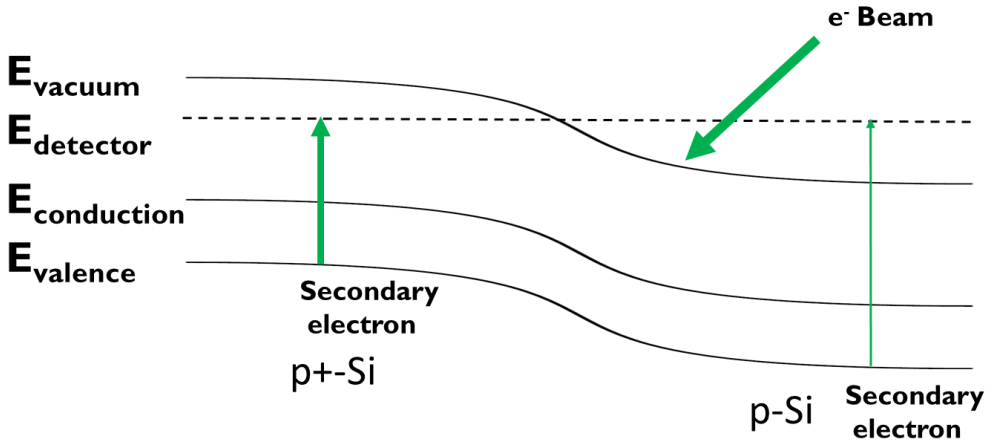

Fig. 6.10 Principle of contrast between p^+ and p Si under SEM

The contrast between p and p^+ Si can be adjusted by several parameters of SEM. The parameters include the accelerating voltage of the incident electron beam, the bias applied to Si and the surface condition of the Si sample…etc [58,59].

Accelerating voltage of the incident electron beam

The high accelerating voltage of the incident electron beam will excite many electron-hole pairs. If the density of excited carriers exceeds the original density of carriers of Si, the Si will perform the intrinsic properties and the contrast between p and p^+ Si decreases. On the other hand, the low accelerating voltage could cause larger spreading of energy for

the incident electron beam, which results in the spherical aberration. Then the SEM image becomes blurred. The optimal accelerated voltage of the incident electron beam is around 1 kV for the p and p^+ Si contrast in the Si solar cell.

The bias applied to Si

The bias applied to Si will affect the band bending between p Si and p^+ Si. As Fig. 6.10, if the bias can be applied between p^+ and p Si to increase the band bending, the energy requirement difference of secondary electrons to reach detector between p and p^+ Si increases, which will result in the images with higher contrast between p and p^+ Si. If the band bending decreases after applying the bias, the contrast between p and p^+ Si decreases.

The surface condition of Si

The roughness of Si surface will create contrasts on SEM images. These contrasts can interference the contrast between p and p^+ Si. As a result, the surface of the Si sample should be polished to eliminate the roughness of the surface and enhance the p and p^+ Si contrast.

Fig. 6.11(a) is the SEM image for the Si part from c-Si solar cells with 0 min, 10 min, 20min NaOH etch. The brighter region in the image is the BSF p^+ Si. The thickness of BSF p^+ Si decreases as etch time increases. Fig. 6.11(b) shows the average BSF p^+ Si thickness for each etch time. The error bars show 95% confidence for the overall average thickness of BSF p^+ Si. Since Si thickness is the linear function of the etch time in 3% NaOH solution at 50℃, these data are fitted by a linear equation. From the equation, when the thickness of BSF p^+ Si is zero, the etch time is ~24 min. As a result, the etch time for the complete removal of the heavily doped Si is around 24 min to 30 min. From the result, at least 91% of Si which is solar grade Si can be recovered for 30 min etch.

(a)

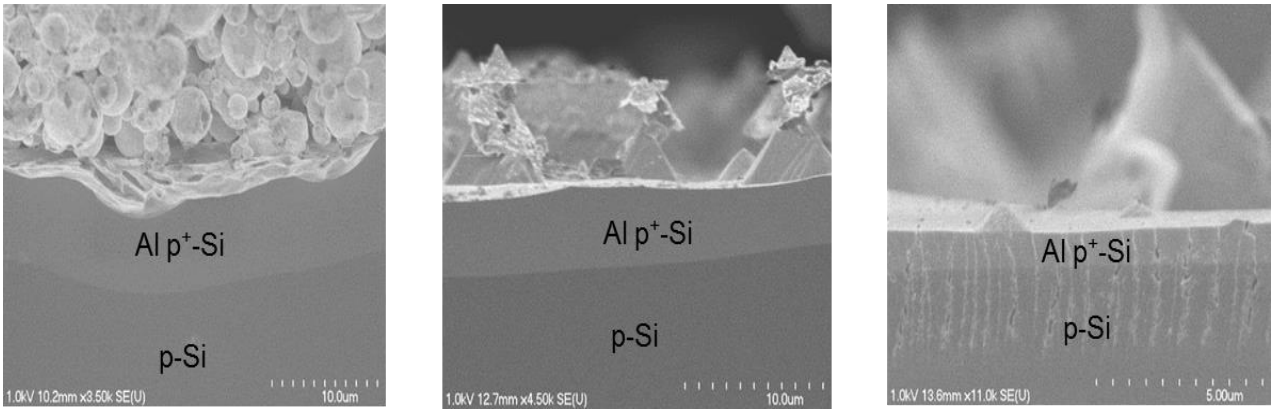

(b)

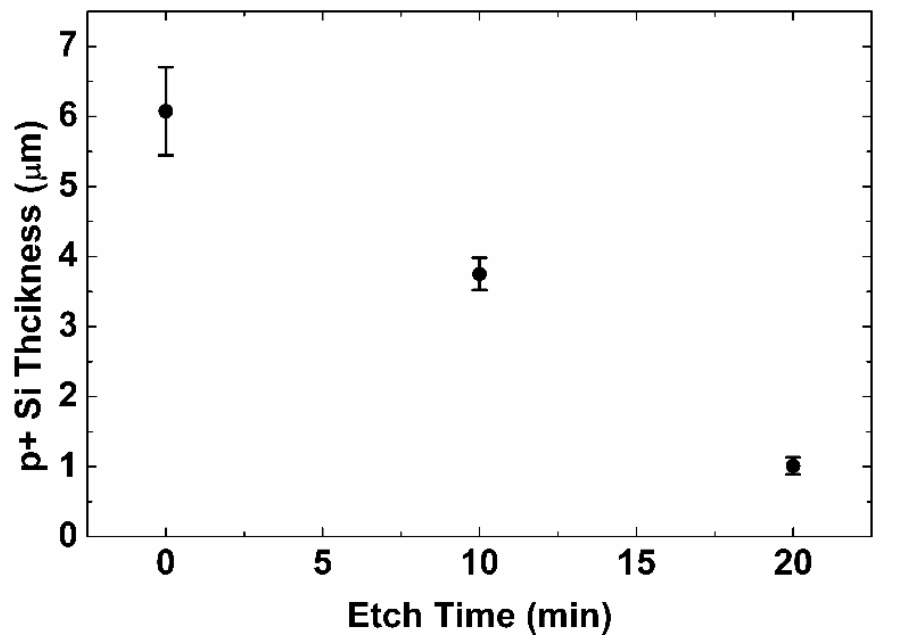

Fig. 6.11 SEM images for BSF p^+ and p Si contrast under different NaOH etch time (a) the average BSF p^+ Si thickness versus etch time (b)

6.5 Characterization of ECV on BSF

Electrochemical capacitance-voltage (ECV) is a technique which is used for the characterization of the carrier density profile. The voltage is applied to form the depletion region on the semiconductor specimen to measure the carrier density. The profile can be achieved by measuring C-V with etching into the specimen electrolytically.

The Si part of a c-Si solar cell with 30 min NaOH etch is used for back surface field p^+ Si characterization by ECV. The electrolyte used is 0.1 M NH_4F/HF [60]. The I-V curve is measured to confirm the voltage range for the depletion without current leakage. Fig. 6.12 is the I-V curve for the sample. The range without leakage current is about -1.2V to -0.4V, which is the voltage range to create the depletion region in the sample. The sign of the voltage in Fig. 6.12 is opposite to the real applied voltage on the sample so more negative voltage will create a deeper depletion region in the p-type Si sample.

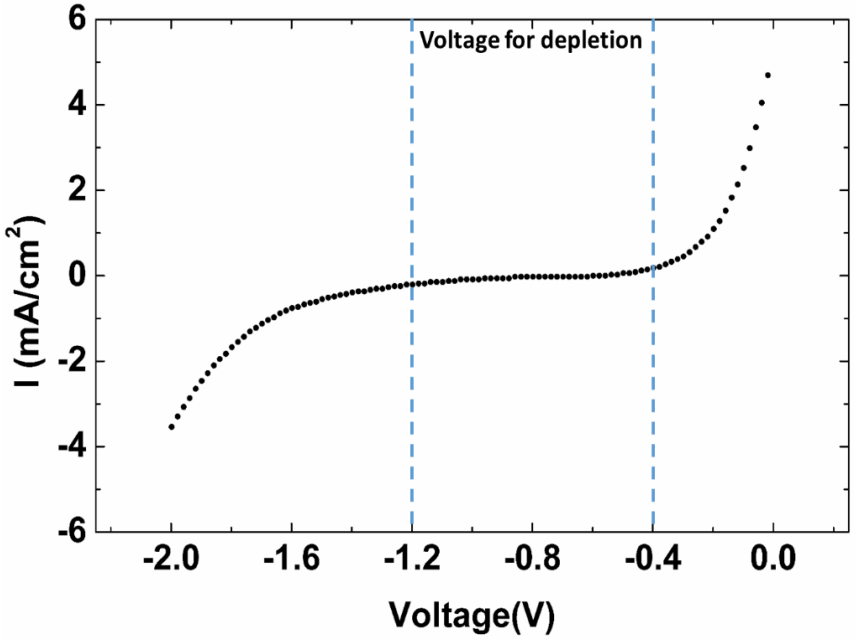

Fig. 6.12 I-V curve of Si part in the c-Si solar cell after 30 min NaOH etch.

The capacitance of the sample is also measured over a range of voltages. Fig. 6.13 is the capacitance measurement and $1/C^2$. From -0.4 V, the sample starts to be depleted. At around -0.5 to -0.8 V, the flat band voltage is in the range and then the depletion condition is sustained between -0.8 V to -1.2V.

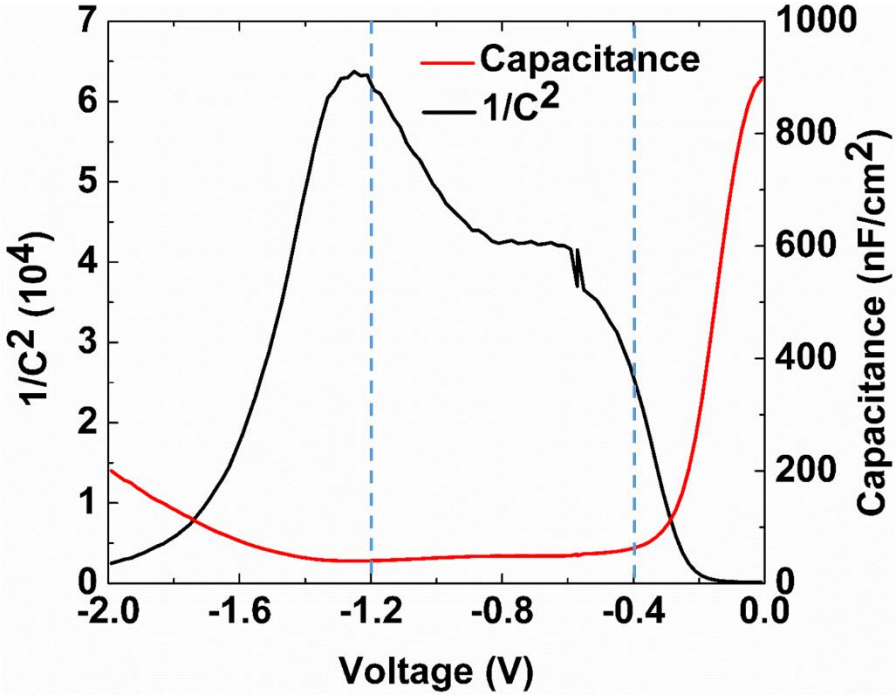

Fig. 6.13 Capacitance measurement for Si part of c-Si solar cells with 30 min NaOH etch.

The voltage chosen for ECV is -1 V for stable measurement since the measurement voltage too close to flat band voltage often showed a discrepancy between the measured doping concentrations by ECV and SIMS data. The profile which is shallower than the depletion depth created by -1 V can be achieved by C-V measurement. Fig. 6.14 is the carrier profile measurement by C-V and ECV. The red points are the C-V data which are measured under the voltage more positive than -0.4 V. As a result, the red points are inaccurate data. The accurate data is not achieved until the depth is deeper than 200 nm.

Between 200 nm and 300 nm, the data are from accurate C-V which is measured under the voltage range between -0.4 V and -1 V. The data from the region which is deeper than 300 nm are measured by ECV with constant -1 V plus etching the contact area with the electrolyte on the sample. From the overall results, the solar grade Si whose doping concentration is about 10^{16} cm^{-3} exists in the region deeper than 200 nm. However, for the depth shallower than 200 nm, the carrier or doping density can not be sure since the data from C-V measurement is not accurate because the measurement voltage is beyond the range of that resulting in depletion condition on the sample. As a result, the ECV measurement can not identify whether the BSF p^+ Si is removed

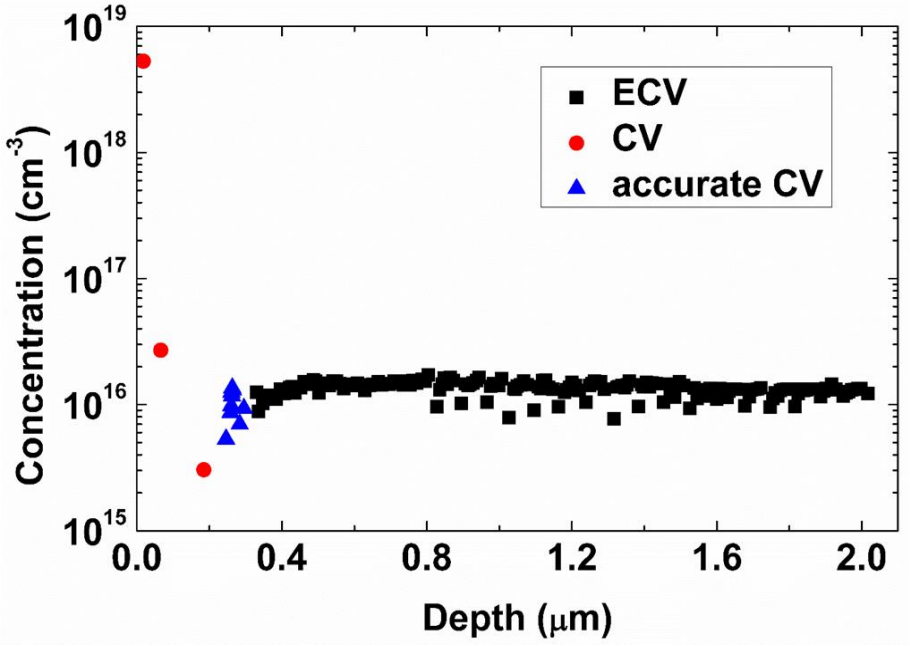

Fig. 6.14 Carrier profile of Si part of c-Si solar cells after 30 min NaOH etch

6.6 Summary

Solar grade Si can be recovered with high recovery rate, at least 91% Si from the cell as the solar grade Si in 30 min by the wet etch process to remove the heavily doped Si in a c-Si solar cell. NaOH is chosen as etch solution due to its cost and reasonable etch rate. The etch mechanism for Si by NaOH is studied and the etch rate for Si is optimized. The 4-point probe is selected as the method for monitoring the etch process due to its convenience for high throughput. SEM contrast for BSF p^+ Si and p Si further proves all the heavily doped Si removal. The NaOH waste can be neutralized by the HNO_3 waste left from metal recycling to lower the danger of final waste.

CHAPTER 7

CONCLUSION

A recycling process is proposed for c-Si solar modules that is technically, environmentally and financially sustainable. It is a three-step process, module recycling, cell recycling and waste handling, to break down Si modules and recover various materials. Over 95% of a module by weight can be recovered by the proposed process including all the glass, Al frame, polymers (as heat source), junction box, ~90% of the Si as solar-grade Si and over 90% of the valuable and toxic metals. Two new technologies are demonstrated to enable the practice of the proposed recycling process. One is sequential electrowinning which allows multiple metals to be recovered one by one from Si modules, Ag, Pb, Cu and Sn. The recovery rates of Ag and Cu are currently 74% and 83%, respectively, but can be increased to 95%. The purity of the recovered metals is above 99%. The other technology is sheet resistance monitoring which maximizes the amount of solar-grade Si recovered from the modules. Over 90% of the Si in the original modules can be recovered, and the recovered Si meets the specifications for solar-grade Si. The recovered metals and Si are new feedstocks to the solar industry and generate over $12/module in revenue at today's prices for Ag and solar-grade Si. This revenue eliminates a major obstacle to Si module recycling, enabling a profitable recycling business without any government support. The chemicals for recycling are carefully selected so their wastes can neutralize each other for a minimal environmental impact. A network for collecting end-of-life solar modules is proposed based on the current distribution network for solar modules to contain the collection cost.

REFERENCES

[1] International Energy Agency, Renewables 2017, (2017). https://www.iea.org/publications/renewables2017/.

[2] Fraunhofer ISE, Photovoltaics Report, 2017.

[3] Z.Campeau, M.Mikofski PhD, E.Hasselbrink PhD, Y.-C.Shen PhD, D.Kavulak PhD, A.Terao PhD, R.Lacerda, W.Caldwell PhD, M.Anderson PhD, Z.Defreitas, D.Degraaff PhD, A.Budiman PhD, L.Leonard, SunPower Module Degradation Rate, (2013).

[4] J.Lindroos, H.Savin, Review of light-induced degradation in crystalline silicon solar cells, Sol. Energy Mater. Sol. Cells. 147 (2016) 115–126. doi:10.1016/j.solmat.2015.11.047.

[5] D.C.Jordan, S.R.Kurtz, Photovoltaic degradation rates - An Analytical Review, Prog. Photovoltaics Res. Appl. 21 (2013) 12–29. doi:10.1002/pip.1182.

[6] H.K.Raut, V.A.Ganesh, A.S.Nair, S.Ramakrishna, Anti-reflective coatings: A critical, in-depth review, Energy Environ. Sci. 4 (2011) 3779. doi:10.1039/c1ee01297e.

[7] C.Battaglia, A.Cuevas, S.DeWolf, High-efficiency crystalline silicon solar cells: status and perspectives, Energy Environ. Sci. 9 (2016) 1552–1576. doi:10.1039/C5EE03380B.

[8] Y.Wan, K.R.Mcintosh, A.F.Thomson, Y.Wan, K.R.Mcintosh, A.F.Thomson, Characterisation and optimisation of PECVD SiNx as an antireflection coating and passivation layer for silicon solar cells, AIP Adv. 3 (2013) 32113. doi:10.1063/1.4795108.

[9] A.G.Aberle, Overview on SiN surface passivation of crystalline silicon solar cells,

Sol. Energy Mater. Sol. Cells. 65 (2001) 239–248. doi:10.1016/S0927-0248(00)00099-4.

[10] W.L.Bailey, M.G.Coleman, C.B.Harris, I.A.Lesk, Texture etching of silicon: method, US4137123 A, 1979. https://www.google.com/patents/US4137123.

[11] PV CYCLE, (n.d.). http://www.pvcycle.org.

[12] P.R.Dias, M.G.Benevit, H.M.Veit, Photovoltaic solar panels of crystalline silicon: Characterization and separation, Waste Manag. Res. 34 (2016) 235–245. doi:10.1177/0734242X15622812.

[13] G.Granata, F.Pagnanelli, E.Moscardini, T.Havlik, L.Toro, Recycling of photovoltaic panels by physical operations, Sol. Energy Mater. Sol. Cells. 123 (2014) 239–248. doi:10.1016/j.solmat.2014.01.012.

[14] T.M.Bruton, R.D.W.Scott, J.P.Nagle, Recycling of high value, high energy content components of silicon PV modules, in: Proc. 12th Eur. Photovolt. Sol. Energy Conf., Amsterdam, 1994: pp. 459–463.

[15] T.Doi, I.Tsuda, H.Unagida, A.Murata, K.Sakuta, K.Kurokawa, Experimental study on PV module recycling with organic solvent method, Sol. Energy Mater. Sol. Cells. 67 (2001) 397–403. doi:10.1016/S0927-0248(00)00308-1.

[16] Y.Kim, J.Lee, Dissolution of ethylene vinyl acetate in crystalline silicon PV modules using ultrasonic irradiation and organic solvent, Sol. Energy Mater. Sol. Cells. 98 (2012) 317–322. doi:10.1016/j.solmat.2011.11.022.

[17] J.R.Bohland, I.I.Anisimov, Possibility of recycling silicon PV modules, 26th Photovolt. Spec. Conf. (1997) 1173–1175. doi:10.1109/PVSC.1997.654298.

[18] D.-W.Zeng, M.Born, K.Wambach, Pyrolysis of EVA and its application in recycling of photovoltaic modules., J. Environ. Sci. (China). 16 (2004) 889–893.

[19] L.Frisson, K.Lieten, K.Declercq, J.Szlufcik, H.deMoor, M.Goris, a.Benali, O.Aceves, Recent improvements in industrial PV module recycling, 16th Eur. Photovolt. Sol. Energy Conf. (2000) 1–4.

[20] P.Dias, S.Javimczik, M.Benevit, H.Veit, Recycling WEEE: Polymer characterization and pyrolysis study for waste of crystalline silicon photovoltaic modules, Waste Manag. 60 (2017) 716–722. doi:10.1016/j.wasman.2016.08.036.

[21] I.Rover, K.Wambach, W.Weinreich, G.Roewer, K.Bohmhammel, Process controlling of the etching system HF/HNO3/H2O, in: Proc. 20th Eur. Photovolt. Sol. Energy Conf., Barcelona, 2005.

[22] E.Klugmann-Radziemska, P.Ostrowski, Chemical treatment of crystalline silicon solar cells as a method of recovering pure silicon from photovoltaic modules, Renew. Energy. 35 (2010) 1751–1759. doi:10.1016/j.renene.2009.11.031.

[23] E.Klugmann-Radziemska, P.Ostrowski, K.Drabczyk, P.Panek, M.Szkodo, Experimental validation of crystalline silicon solar cells recycling by thermal and chemical methods, Sol. Energy Mater. Sol. Cells. 94 (2010) 2275–2282. doi:10.1016/j.solmat.2010.07.025.

[24] J.Park, N.Park, Wet etching processes for recycling crystalline silicon solar cells from end-of-life photovoltaic modules, RSC Adv. 4 (2014) 34823–34829. doi:10.1039/C4RA03895A.

[25] S.Kang, S.Yoo, J.Lee, B.Boo, H.Ryu, Experimental investigations for recycling of silicon and glass from waste photovoltaic modules, Renew. Energy. 47 (2012) 152–159. doi:10.1016/j.renene.2012.04.030.

[26] W.-H.Huang, M.Tao, A simple green process to recycle Si from crystalline-Si

solar cells, in: 2015 IEEE 42nd Photovolt. Spec. Conf. PVSC 2015, 2015. doi:10.1109/PVSC.2015.7356259.

[27] A.Muller, I.Rover, K.Wambach, D.vonRamin-Marro, Recovery of high value material of different photovoltaic technologies, in: Proc. 22nd Eur. Photovolt. Sol. Energy Conf., Milan, 2007: pp. 2613–2616.

[28] W.-H.Huang, W.J.Shin, L.Wang, M.Tao, Recovery of valuable and toxic metals from crystalline-Si modules, in: Conf. Rec. IEEE Photovolt. Spec. Conf., 2016. doi:10.1109/PVSC.2016.7750344.

[29] USGS, Mineral Commodity Summaries, 2017.

[30] M.Tao, Terawatt Solar Photovoltaics: Roadblocks and Opportunities, London, Springer, 2014.

[31] C.S.Tao, J.Jiang, M.Tao, Natural resource limitations to terawatt-scale solar cells, Sol. Energy Mater. Sol. Cells. 95 (2011) 3176–3180. doi:10.1016/j.solmat.2011.06.013.

[32] A.Müller, K.Wambach, E.Alsema, Life Cycle Analysis of Solar Module Recycling Process, MRS Proc. 895 (2005) 895-G03-7. doi:10.1557/PROC-0895-G03-07.

[33] V.Fthenakis, P.Moskowitz, Photovoltaics: environmental, health and safety issues and perspectives, Prog. Photovoltaics Res. …. 38 (2000) 27–38. http://www.calepa.ca.gov/Cepc/2010/AsltonBird/AppAEx7.pdf.

[34] M.Tammaro, A.Salluzzo, J.Rimauro, S.Schiavo, S.Manzo, Experimental investigation to evaluate the potential environmental hazards of photovoltaic panels, J. Hazard. Mater. 306 (2016) 395–405. doi:10.1016/j.jhazmat.2015.12.018.

[35] V.M.Fthenakis, End-of-life management and recycling of PV modules, Energy Policy. 28 (2000) 1051–1058. doi:10.1016/S0301-4215(00)00091-4.

[36] T.Y.Wang, J.C.Hsiao, C.H.Du, Recycling of materials from silicon base solar cell module, Conf. Rec. IEEE Photovolt. Spec. Conf. (2012) 2355–2358. doi:10.1109/PVSC.2012.6318071.

[37] USDA, Supplemental Technical Report for Sodium Nitrate, (2011).

[38] K.Van denBroeck, N.VanHoornick, J.VanHoeymissen, R.DeBoer, A.Giesen, D.Wilms, Sustainable treatment of HF wastewaters from semiconductor industry with a fluidized bed reactor, IEEE Trans. Semicond. Manuf. 16 (2003) 423–428. doi:10.1109/TSM.2003.815624.

[39] P.E.Aqueveque, E.P.Wiechmann, J.Herrera, E.J.Pino, Measurable variables in copper electrowinning and their relevance to predicting process performance, IEEE Trans. Ind. Appl. 51 (2015) 2607–2614. doi:10.1109/TIA.2014.2377298.

[40] M.Moats, M.Free, A bright future for copper electrowinning, JOM. 59 (2007) 34–36. doi:10.1007/s11837-007-0128-y.

[41] N.T.Beukes, J.Badenhorst, Copper electrowinning: Theoretical and practical design, J. South. African Inst. Min. Metall. 109 (2009) 343–356.

[42] C.Anderson G, Optimization of Industrial Copper Electro Winning Solutions, J. Adv. Chem. Eng. 7 (2017) 1–3. doi:10.4172/2090-4568.1000156.

[43] F.Vegliò, R.Quaresima, P.Fornari, S.Ubaldini, Recovery of valuable metals from electronic and galvanic industrial wastes by leaching and electrowinning, Waste Manag. 23 (2003) 245–252. doi:10.1016/S0956-053X(02)00157-5.

[44] D.K.Schroder, Semiconductor material and device characterization, John Wiley & Sons, 2006.

[45] K.Yoo, J.Lee, K.Lee, B.Kim, M.Kim, S.Kim, B.D.Pandey, Recovery of Sn, Ag and Cu from Waste Pb-Free Solder Using Nitric Acid Leaching, Mater. Trans. 53 (2012) 2175–2180. doi:10.2320/matertrans.M2012268.

[46] A.Mecucci, K.Scott, Leaching and electrochemical recovery of copper, lead and tin from scrap printed circuit boards, J. Chem. Technol. Biotechnol. 77 (2002) 449–457. doi:10.1002/jctb.575.

[47] Bine Information Service, Recycling Photovoltaic Modules, 2010.

[48] IC Fabrication Technology from 60s to date_Part 1, (n.d.). https://archive.cnx.org/contents/9583ee74-d153-4059-9239-5976da5a9589@2/chapter-6-ic-fabrication-technology-from-60s-to-date-part-1.

[49] A.Kaminski, B.Vandelle, A.Fave, J.P.Boyeaux, L.Q.Nam, R.Monna, D.Sarti, A.Laugier, Aluminium BSF in silicon solar cells, Sol. Energy Mater. Sol. Cells. 72 (2002) 373–379. doi:10.1016/S0927-0248(01)00185-4.

[50] B.Sopori, V.Mehta, P.Rupnowski, H.Moutinho, A.Shaikh, C.Khadilkar, M.Bennett, D.Carlson, Studies on Backside Al-Contact Formation in Si Solar Cells: Fundamental Mechanisms, MRS Proc. 1123 (2011) 7–11. doi:10.1557/PROC-1123-1123-P07-11.

[51] C.H.Lin, S.Y.Tsai, S.P.Hsu, M.H.Hsieh, Structural properties of the solidified-Al/regrown-Si structures of printed Al contacts on crystalline Si solar cells, Sol. Energy Mater. Sol. Cells. 92 (2008) 986–991. doi:10.1016/j.solmat.2008.02.031.

[52] V.Meemongkolkiat, K.Nakayashiki, D.S.Kim, R.Kopecek, A.Rohatgi, Factors Limiting the Formation of Uniform and Thick Aluminum–Back-Surface Field and Its Potential, J. Electrochem. Soc. 153 (2006) G53. doi:10.1149/1.2129106.

[53] T.Lauermann, B.Fröhlich, G.Hahn, Terheiden Barbara, Diffusion-based model of local Al back surface field formation for industrial passivated emitter and rear cell solar cells, Prog. PHOTOVOLTAICS. 23 (2015) 10–18.

[54] J.Acker, T.Koschwitz, B.Meinel, R.Heinemann, C.Blocks, HF/HNO3etching of the saw damage, Energy Procedia. 38 (2013) 223–233. doi:10.1016/j.egypro.2013.07.271.

[55] M.Steinert, J.Acker, S.Oswald, K.Wetzig, Study on the mechanism of silicon etching in HNO3-rich HF/HNO3 mixtures inf, J. Phys. Chem. C. 111 (2007) 2133–2140. doi:10.1021/jp066348j.

[56] M.Steinert, J.Acker, A.Henßge, K.Wetzig, Experimental Studies on the Mechanism of Wet Chemical Etching of Silicon in HF/HNO[sub 3] Mixtures, J. Electrochem. Soc. 152 (2005) C843. doi:10.1149/1.2116727.

[57] S.Franssila, Introduction to microfabrication, John Wiley & Sons, 2010.

[58] S.L.Elliott, R.F.Broom, C.J.Humphreys, Dopant profiling with the scanning electron microscope - A study of Si, J. Appl. Phys. 91 (2002) 9116–9122. doi:10.1063/1.1476968.

[59] C.P.Sealy, M.R.Castell, P.R.Wilshaw, Mechanism for secondary electron dopant contrast in the SEM, J. Electron Microsc. (Tokyo). 49 (2000) 311–321. doi:10.1093/oxfordjournals.jmicro.a023811.

[60] E.Başaran, Choice of electrolyte for doping profiling in Si by electrochemical C-V technique, Appl. Surf. Sci. 172 (2001) 345–350. doi:10.1016/S0169-4332(00)00871-0.